Solid-fluid phase transition of quantum hard spheres at finite temperatures

Karl J. Runge
Courant Institute of Mathematical Sciences, New York University, 251 Mercer Street, New York, New York 10012

Geoffrey V. Chester
Laboratory of Atomic and Solid State Physics, Cornell University, Ithaca, New York 14853
(Received 3 February 1988)

Path-integral Monte Carlo simulation is used to study a system of distinguishable quantum hard spheres at finite temperatures. Extensive tables of the energy and pressure in the fluid and fcc solid phases are presented along with a careful study of the convergence of these properties with "time-slice discretization." The Helmholtz free energy in the solid phase is computed via a thermodynamic integration that continuously transforms the system into a harmonic Einstein crystal. The free energy in the solid is compared to that computed by the Debye model. Input data for the Debye model is provided by performing Monte Carlo computations of the elastic moduli, C_{11}, C_{12}, and C_{44} at $T=0$. The two methods of computing the free energy are in qualitative agreement, with some uncertainty induced by the lack of dispersion in the phonon spectrum, $\omega(k)$, in the Debye model. The solid-fluid phase transition is located along three isotherms, that correspond to 4, 10, and 20 K in a simple mapping of the hard-sphere system onto ^{4}He. From these data we postulate a generalization of Lindemann's melting criterion for quantum systems at finite temperatures. The hard-sphere free energy and pair distribution functions are used to predict the equations of state and freezing transition in ^{3}He and ^{4}He via a first-order perturbation theory. The liquid-vapor phase transition of ^{4}He at 4 K is located as well. The agreement between these predictions and experiment is very good, except at very high density where a more sophisticated choice of hard-sphere reference system is required.

I. INTRODUCTION

During the history of Monte Carlo simulation the hard-sphere system has been remarkably durable. The form of the interaction, zero potential energy if no pair of spheres overlap and infinite otherwise, makes the system a simple, but realistic, model of interacting atoms or spherical molecules, as well as a very straightforward problem computationally. Metropolis, Rosenbluth, Rosenbluth, Teller, and Teller[1] studied the classical system of hard spheres in the first important test of their extremely powerful sampling algorithm (to be referred to here as MRRTT) that has proved so important in simulation studies in statistical mechanics. Hoover and Ree[2] were the first to locate the thermodynamic phase transition between the solid and fluid states of the classical system. The first "exact" simulation study of the quantum-mechanical ground state of Bose hard spheres was performed by Kalos, Levesque, and Verlet[3] using the technique of Green's-function Monte Carlo (GFMC) in which the melting transition was located by computing the energy of the solid and fluid phases. Our work attempts to bridge the gap between the high-temperature, classical results of Hoover and Ree and the ground-state, $T=0$, study of Kalos *et al.*, by providing the equation of state, structural properties, and the location of the solid-fluid phase transition for quantum-mechanical hard spheres at finite temperatures along several isotherms.

In our work we have assumed the hard spheres obey Boltzmann (distinguishable particle) statistics, which proves to be of great computational convenience because particle exchanges need not be considered.[4] We have chosen the temperature high enough so that the corrections due to Bose or Fermi statistics are small, although the system is still strongly quantum mechanical. This situation can be achieved in strongly repulsive systems because the corrections due to statistics involve particle exchanges and can be shown to go to zero exponentially with increasing temperature. On the other hand, corrections from "diffraction effects" (of wave mechanics) vanish only as an inverse power of the temperature in the classical limit $T\rightarrow\infty$.[5,6] There, therefore, exists a rather large range of temperature where the system is quantal and yet the statistics of the particles play a very minor role. It is easy to show that in this regime Bose, Fermi, and Boltzmann systems governed by the same Hamiltonian will all have identical structural and thermodynamical properties.[7] Furthermore, it is almost certainly true that in the solid phase of strongly repulsive systems the influence of statistics is negligible for *all* temperatures.[8] This belief follows from the observation that the solid phase is relatively "crowded": particle exchanges are extremely infrequent.[9]

The paper is organized as follows. In Sec. II the problem to be studied is defined and the path-integral representation of it is outlined. The interpretation of the quantum path integral as an "effective" classical system is also discussed in this section. Three important computational details are described in Sec. III: the short (imaginary) time approximation for each "step" in the path integral; the choice of the random Markov process to sample paths of the system; and the thermodynamic integra-

tion techniques to compute the free energy of the system. In Sec. IV we discuss our computational results for the equation of state and the structure of the hard-sphere solid and fluid phases. The data include tables of the energy, pressure, free energy, and pair-distribution function in both phases and Lindemann's ratio for the solid. Analytic fits to the density dependence of the energy and pressure are provided as well. We also present a study of the elastic properties, the location of the freezing transition, and a comparison of the structural results at $T>0$ with ground-state GFMC studies of hard spheres and realistic models of helium. In Sec. V we demonstrate that a first-order perturbative scheme employing the finite-temperature hard spheres as a reference system can be successfully used to study the equations of state and phase diagrams of ^{3}He and ^{4}He.

II. PATH INTEGRALS

In this section we define the problem to be investigated and develop its path-integral representation. Consider N distinguishable particles in a periodic box of volume V. Let R denote the positions of all the particles: $R=(\mathbf{r}_1,\ldots,\mathbf{r}_N)$. The nonrelativistic Hamiltonian for the system shall be taken as

$$H=\sum_{i=1}^{N}\frac{-\hbar^2}{2m}\nabla_i^2+U(R)\ , \tag{1}$$

where

$$U=\sum_{(i,j)}v(r_{ij})\ .$$

The mass of each particle is m, the sum in the potential energy U is over all pairs of particles (i,j), and r_{ij} is the distance between particles i and j (actually the minimum distance between the particles and all of their periodic images). For the hard-sphere system $v(r)$ is given by

$$v(r)=\begin{cases}0, & r>\sigma\\ \infty, & r<\sigma\ ,\end{cases} \tag{2}$$

where σ is the hard-sphere diameter.

Our goal is to study the equilibrium statistical mechanics of the above system. Let β denote the inverse temperature, $1/k_BT$, where k_B is Boltzmann's constant. The partition function of the system is defined by

$$Z=\mathrm{Tr}(e^{-\beta H}) \tag{3}$$

which is related to the Helmholtz free energy by $F(N,V,T)=-k_BT\ln(Z/N!)$. The average of an operator B is given by

$$\langle B\rangle=\frac{1}{Z}\mathrm{Tr}(Be^{-\beta H})\ . \tag{4}$$

The trace in the above equations is over a basis of quantum states with the appropriate symmetry and boundary conditions: for Boltzmann statistics the sum is over states of all symmetry, whereas for Bose or Fermi statistics one would sum only over totally symmetric or totally antisymmetric states, respectively.

The density matrix in the coordinate representation, $\rho(R,R',\beta)$, is given by the matrix element

$$\rho(R,R',\beta)=\langle R\mid e^{-\beta H}\mid R'\rangle\ . \tag{5}$$

This function is often referred to as the propagator of the system in imaginary time β because of its similarity to the time evolution operator e^{iHt} of ordinary quantum mechanics. If the trace in Eq. (3) is performed in the coordinate representation basis we obviously have

$$Z=\int dR\,\rho(R,R,\beta)\ , \tag{6}$$

where the integral implies integration of every coordinate over the volume

$$\int dR\leftrightarrow\int_V d\mathbf{r}_1\cdots\int_V d\mathbf{r}_N\ .$$

Since the integral (6) is formally equivalent to a classical system with Boltzmann factor

$$e^{-U_{\mathrm{eff}}(R)}\equiv\rho(R,R,\beta)\ , \tag{7}$$

if one knew $\rho(R,R,\beta)$ as a function of R, then one could imagine using the standard simulation techniques for classical systems (MRRTT, for example) to study the quantum system. Unfortunately, for interacting systems one does not know the density matrix exactly for *any* nonzero inverse temperature β. To proceed further we resort to path integrals.

Following the standard derivation of the path integral,[10,11] one uses completeness,

$$\int dR\mid R\rangle\langle R\mid=1$$

to arrive at the identity

$$\rho(R,R',\beta)=\int dR_1\cdots\int dR_{M-1}\rho(R,R_1,\tau)\cdots\rho(R_{M-1},R',\tau)\ , \tag{8}$$

where $\tau=\beta/M$. This identity is found by inserting $M-1$ complete sets between the M factors in $e^{-\beta H}=(e^{-\tau H})^M$. For fixed β, one notes that in the limit $M\to\infty$, τ corresponds to very high temperatures or very short imaginary times. Not surprisingly, one may "expand" about the classical result ($\tau=0$) to arrive at accurate expressions for $\rho(R,R',\tau)$ when τ is small.

The simplest high-temperature approximation is the "primitive approximation":[11]

$$\rho(R,R',\tau)\approx\langle R\mid e^{-\tau K}\mid R'\rangle[e^{-(1/2)\tau[U(R)+U(R')]}+O(\tau^3)]\ , \tag{9}$$

where K denotes the kinetic energy operator of the system. The matrix element involving the kinetic energy is simply the ideal gas propagator and is given by[10]

$$\langle R \mid e^{-\tau K} \mid R' \rangle = \left[\frac{M}{2\pi\lambda_T^2} \right]^{3N/2} \times \exp\left[-\frac{M}{2\lambda_T^2} \sum_{i=1}^{N} (\mathbf{r}_i - \mathbf{r}_i')^2 \right] , \quad (10)$$

with the de Broglie thermal wavelength defined by

$$\frac{\hbar^2}{m\lambda_T^2} = k_B T = \frac{1}{\beta} .$$

We shall use the notation $(R-R')^2$ to denote terms like $\sum_{i=1}^{N}(\mathbf{r}_i - \mathbf{r}_i')^2$ in Eq. (10).

Although the primitive approximation is not used in this work (see Sec. III), we shall display its use in the path integral since it clearly demonstrates the structure of the probability distribution used in path-integral Monte Carlo (PIMC). If one uses Eq. (10) in Eq. (9) and substitutes the result into expression (8), one gets the following for the partition function:

$$Z \approx \int dR_1 \cdots dR_M e^{-U_{\text{eff}}(R_1, \ldots, R_M)} , \quad (11)$$

where

$$e^{-U_{\text{eff}}(R_1, \ldots, R_M)} \equiv \left[\frac{M}{2\pi\lambda_T^2} \right]^{3NM/2} \exp\left[-\frac{M}{2\lambda_T^2} \sum_{l=1}^{M} (R_l - R_{l+1})^2 \right] \exp\left[-\tau \sum_{l=1}^{M} U(R_l) \right]$$

(note that $R_{M+1} \equiv R_1$). In its present approximate form, we now know analytically the integrand in Eq. (11) and (8) as a function of $R_1, \ldots, R_M$. The positivity of the integrand implies that the quantum problem we want to solve is formally equivalent to a *classical* system consisting of $3NM$ coordinates, $R_1, \ldots, R_M$, with a potential energy of interaction U_{eff}. As has been noted many times,[12] the equivalent classical system resembles a system of N classical ring polymers each consisting of M monomers. A single polymer is actually the quantum path of a particle in three-space. The intrapolymer interaction originates from the kinetic energy term in Eq. (9) and is given by harmonic forces with spring constant M/λ_T^2. The interpolymer interaction comes from the potential-energy term in Eq. (9) and is the sum of $\tau U(R_l)$ over each "time" index l. As opposed to real polymers, the interpolymer interaction here acts only between monomers with the *same* time index l.

One may now use the standard technique of MRRTT to simulate the classical system of polymers. Let $\mathcal{R}$ be shorthand for $R_1, \ldots, R_M$: it denotes one configuration of the N polymers (in other words, a discretized path of the system through configuration space). The simulation will give rise to a collection of paths $\{\mathcal{R}\}$ sampled from the normalized probability distribution

$$\mathcal{P}(\mathcal{R}) = \frac{1}{Z} e^{-U_{\text{eff}}(\mathcal{R})} . \quad (12)$$

The collection may then be used to compute thermodynamic averages. Suppose, for example, one is interested in estimating the average energy $\langle H \rangle$ of the quantum system. One has

$$E \equiv \langle H \rangle = -\frac{\partial}{\partial\beta} \ln Z , \quad (13)$$

and so

$$E = \langle \hat{E}(\mathcal{R}) \rangle , \quad (14)$$

where

$$\hat{E}(\mathcal{R}) = \frac{\partial}{\partial\beta} U_{\text{eff}}(\mathcal{R}) . \quad (15)$$

The average of a function $B(\mathcal{R})$ is defined by[13]

$$\langle B(\mathcal{R}) \rangle = \frac{1}{Z} \int d\mathcal{R}\, B(\mathcal{R}) e^{-U_{\text{eff}}(\mathcal{R})} = \int d\mathcal{R}\, B(\mathcal{R}) \mathcal{P}(\mathcal{R}) . \quad (16)$$

Precisely as is done in classical simulations, one constructs an estimate for $\langle B(\mathcal{R}) \rangle$ by taking the arithmetic mean of $B(\mathcal{R})$ evaluated at each $\mathcal{R}$ in the collection $\{\mathcal{R}\}$. As usual, the error in this estimate goes as the inverse square root of the number of "independent" configurations in $\{\mathcal{R}\}$. Although we have only considered the estimation of the total energy in the above example, the construction of observables for other properties (e.g., kinetic energy, potential energy, pressure, pair-distribution function, and Lindemann parameter) is relatively straightforward, and will be discussed in the next section.

Before closing this section, we note a few points. In the absence of "interpolymer" interactions ($U=0$ or low density), the size of a path scales as λ_T (it is the width of the Gaussian). With interactions present, this statement will be more or less true until λ_T exceeds the average size of the "cage" that confines each path. On the other hand, as the temperature increases λ_T goes to zero, so that each path collapses to a point and the integrand in (11) reduces to $e^{-\beta U(R)}$, which is the classical limit.

III. COMPUTATIONAL METHOD

The computational techniques required in this work can be broken up into three categories: (a) the choice of high-temperature approximation in the path integral; (b) the choice of Markov transition probability in the MRRTT algorithm; and (c) methods to compute the free energy of the solid and fluid phases. These three items will be discussed in detail in the following subsections, although an understanding of them is not needed to interpret the results presented in Secs. IV and V.

A. High-temperature approximation

Recall that in order to arrive at the large-dimensional integral of the form of Eq. (11), where the integrand is known analytically, one must make some sort of approximation to the short-time propagator. Therefore, one must always perform consistency checks by varying M to see that the results have converged to the $M=\infty$ value. In lieu of this, one must carefully extrapolate the results to $M=\infty$. In order to go to a lower temperature (higher β) and retain the same level of accuracy ($\sim\tau$) one must choose a larger value of M, thereby increasing the computer time required by the calculation.

If the primitive approximation [Eq. (9)] is used in a PIMC simulation of hard spheres, one finds that the rate of convergence of physical properties with M is disappointingly slow. For example, consider the pair-distribution function $g(r)$ that is a measure of the average density of particles a distance r away from one fixed at the origin, and is defined by[5]

$$g(r)=V\left[1-\frac{1}{N}\right]\langle\delta(\mathbf{r}_i-\mathbf{r}_j-\mathbf{r})\rangle \tag{17}$$

for any pair of particles i,j. For hard spheres $g(r)$ goes continuously to zero as $r\to\sigma$ since all eigenfunctions of the Hamiltonian vanish continuously as one brings any pair of spheres to contact. The use of the primitive approximation in a PIMC simulation of hard spheres leads to a $g(\sigma)$ that does not vanish for finite M, but rather goes slowly toward zero as M tends to infinity. Barker[14] and Jacucci and Omerti[15] have performed careful tests of the convergence of physical quantities with M on model systems with "hard" boundary conditions (including the two-hard-sphere system). These authors come to the conclusion that one may enjoy a substantial decrease in the required value of M if the high-temperature approximation incorporates the boundary conditions. All of the results presented in this paper are derived from a high-temperature density matrix with this property.

As suggested by Barker and by Bruch *et al.*,[16] and implemented in many-body simulations by Pollock and Ceperley,[4,17] the following density matrix is much more accurate than the primitive approximation:

$$\rho(R,R',\tau)\approx\langle R\mid e^{-\tau K}\mid R'\rangle\prod_{(i,j)}\tilde{\rho}(\mathbf{r}_{ij},\mathbf{r}'_{ij},\tau)\ , \tag{18}$$

where the first factor is given by Eq. (10) and $\mathbf{r}_{ij}=\mathbf{r}_i-\mathbf{r}_j$. $\tilde{\rho}$ is the exact two-particle density matrix divided by the ideal two-particle density matrix, both at inverse temperature τ,

$$\tilde{\rho}(\mathbf{r}_{ij},\mathbf{r}'_{ij},\tau)=\frac{\rho_2(\mathbf{r}_i,\mathbf{r}_j,\mathbf{r}'_i,\mathbf{r}'_j,\tau)}{\rho_1(\mathbf{r}_i,\mathbf{r}'_i,\tau)\rho_1(\mathbf{r}_j,\mathbf{r}'_j,\tau)}\ , \tag{19}$$

where ρ_2 is the exact two-particle density matrix with potential $v(r)$ and ρ_1 is the one-particle density matrix (ideal gas). Equation (18) is a very good approximation because it has the solution to the quantum two-body problem built into it. The primitive approximation clearly does not have this feature. When used in a PIMC simulation, the density matrix in Eq. (18) will give exact results for two-particle systems even with $M=1$. This fact implies that in a many-body simulation, the resulting equation of state with $M=1$ will be correct to $O(\rho^2)$ at low density ($\rho=N/V$). [Note that Eq. (18) gives the correct second virial coefficient.] These statements are correct for *all* temperatures (although the range of density where the second virial coefficient gives good results goes to zero as $T\to 0$). Bruch *et al.*[16] have studied the density matrix in Eq. (18) with $M=1$ by integral equation techniques and has located the liquid-vapor critical points of ^{3}He and ^{4}He semiquantitatively. For fixed temperature, as the density increases one will need to make larger choices of M because Eq. (18) is not exact. However, for any temperature and density the value of M required for convergence should always be much smaller than that required by the primitive approximation because Eq. (18) contains more information about the quantum problem than Eq. (9) does.

Having discussed the merits of the approximation density matrix (18), we now describe the high-temperature density matrix used in this work. Instead of the exact two-body density matrix mentioned above, we use a convenient analytic approximation to the hard-sphere two-body density matrix known as the "image approximation."[15,18] The approximation follows from the observation that when $\lambda_T/\sqrt{M}\ll\sigma$ (true for small τ), the curvature of the spheres may be neglected. The two-body density matrix ρ_2 is replaced by a free-particle density matrix that vanishes on a tangent plane approximation to the hard-sphere surface. The derivation is discussed by Jacucci[18] and we shall only quote the result:

$$\tilde{\rho}(\mathbf{r},\mathbf{r}',\tau)=1-\exp\left[-\frac{M}{\lambda_T^2}(r-\sigma)(r'-\sigma)\right]\ , \tag{20}$$

with $\tilde{\rho}=0$ if either $r<\sigma$ or $r'<\sigma$.

The path-integral representation used in this paper is found by substituting $\tilde{\rho}$ of Eq. (20) into Eq. (18) and the result into Eq. (8). In this case one gets

$$\begin{aligned}e^{-U_{\text{eff}}(\mathcal{R})}=&\left[\frac{M}{2\pi\lambda_T^2}\right]^{3NM/2}\\&\times\exp\left[-\frac{M}{2\lambda_T^2}\sum_{l=1}^{M}(R_l-R_{l+1})^2\right]\\&\times\prod_{l=1}^{M}\prod_{(i,j)}\tilde{\rho}(\mathbf{r}_{ij}(l),\mathbf{r}_{ij}(l+1),\tau)\ ,\end{aligned} \tag{21}$$

where $\mathcal{R}=(R_1,\ldots,R_M)$ as in Sec. II.

One may next construct estimators for physical observables by taking the appropriate derivatives of the partition function as was done in Eqs. (13) and (15). None of the resulting detailed expressions shall be shown here since the formulas become rather cumbersome.

For the kinetic energy (there is no potential energy in the hard-sphere system) one may take the β derivative of Z:

$$\hat{K}(\mathcal{R})=\frac{\partial}{\partial\beta}U_{\text{eff}}(\mathcal{R})\ . \tag{22}$$

This estimator of the energy shall be referred to as the "β-derivative" estimator. A second estimator for the kinetic energy may be found from the following relation:

$$\langle \nabla_i^2 \rangle = \frac{1}{Z} \int dR \, \nabla_i^2 \rho(R,R',\beta) \Big|_{R'=R} . \tag{23}$$

One may evaluate the Laplacian after substituting the high-temperature approximation into Eq. (8). A factor of $(-\hbar^2/2m)$ multiplied by Eq. (23) is the average kinetic energy of the ith particle, and thus, the sum over all i gives an estimator for the total kinetic energy of the system. Having the two estimators, (22) and (23), proved to be very useful in testing the convergence of our results with M. The two will be equal on average only if M has been taken large enough. Indeed, the Monte Carlo results for the two are observed to come together as M is increased. Because the same set of paths, $\{\mathcal{R}\}$, is used to average both estimators, the systematic *difference* between the two may be estimated with a much smaller statistical error than either estimator by itself.[15] The Monte Carlo results will be discussed in more detail in Sec. IV.

The pressure P of the system is related to a volume derivative of the Helmholtz free energy

$$P = -\frac{\partial F}{\partial V} = k_B T \frac{\partial \ln Z}{\partial V} . \tag{24}$$

By using this equation an estimator for the pressure of the system may be found in the standard fashion.[19] One performs a change of variables in Eq. (11) so that each coordinate ranges over the *unit* cube, the differentiation of the partition function with respect to the volume may then be easily carried out. The resulting derivative of U_{eff} that comes down out of the exponential forms the estimator. Another estimator for P may be found by the use of the virial theorem[20]

$$P = \frac{2}{3}\frac{K}{V} + \rho^2 \left[\frac{\pi\sigma^3\hbar^2}{3m} \right] g''(\sigma) , \tag{25}$$

where $g''(\sigma)$ is the curvature of the pair-distribution function at contact. As with the kinetic energy estimators, Eqs. (24) and (25) give the same value for the pressure in the limit $M \to \infty$. The latter estimator for P was found to be much less accurate than the former, and so none of the pressures derived from it are reported here.

If an operator B is diagonal in the coordinate representation then it is a simple matter to show that its thermal average is equal to the PIMC average of $B(R_1)$. Since all steps along the path are equivalent, one gets

$$\hat{B}(\mathcal{R}) = \frac{1}{M} \sum_{l=1}^{M} B(R_l) \tag{26}$$

as a valid estimator as well. The pair-distribution function, Lindemann's parameter, and any other spatial correction function fall into this category.

B. Choice of transition probability

The MRRTT algorithm allows much freedom in the choice of the random process used to sample a probability distribution $\mathcal{P}(\mathcal{R})$. One should try to choose this random process so that the system samples different regions of configuration space as quickly as possible per unit of computational time. If this can be achieved, the results are more reliable because a larger region of configuration space is sampled and the configurations are more statistically independent. In the following we shall describe our attempt to incorporate the above desirable feature into a Markov random process.

Consider a Markov process with transition probability $\mathcal{T}(\mathcal{R} \to \mathcal{R}')$ that satisfies the equation of "detailed balance"[21]

$$\mathcal{P}(\mathcal{R})\mathcal{T}(\mathcal{R} \to \mathcal{R}') = \mathcal{P}(\mathcal{R}')\mathcal{T}(\mathcal{R}' \to \mathcal{R}) , \tag{27}$$

for all $\mathcal{R}$ and $\mathcal{R}'$. Let $\mathcal{T}$ also have the property that it is possible to get from any $\mathcal{R}$ to any other $\mathcal{R}'$ in a finite number of steps. With these conditions one can prove that, regardless of the starting configuration, if the random process $\mathcal{T}$ is iterated long enough then the configurations will be asymptotically distributed by $\mathcal{P}(\mathcal{R})$.

The choice of transition probability due to MRRTT is of the form

$$\mathcal{T}(\mathcal{R} \to \mathcal{R}') = \mathcal{T}^*(\mathcal{R} \to \mathcal{R}') A(\mathcal{R} \to \mathcal{R}') , \tag{28}$$

where $\mathcal{T}^*$ is an *a priori* transition probability and A is an acceptance probability: One samples a trial configuration $\mathcal{R}'$ from $\mathcal{T}^*(\mathcal{R} \to \mathcal{R}')$ and accepts it with probability $A(\mathcal{R} \to \mathcal{R}')$, otherwise the configuration remains at $\mathcal{R}$. The acceptance probability is given by

$$A(\mathcal{R} \to \mathcal{R}') = \min \left[1, \frac{\mathcal{P}(\mathcal{R}')\mathcal{T}^*(\mathcal{R}' \to \mathcal{R})}{\mathcal{P}(\mathcal{R})\mathcal{T}^*(\mathcal{R} \to \mathcal{R}')} \right] . \tag{29}$$

In the simplest choice for $\mathcal{T}^*$, a single "bead" on one path is selected and a new trial position for it is sampled uniformly in a cube of side length Δ centered about the bead's initial position, and then one accepts the new position with probability A. This process is repeated for each monomer, in turn, many times. Typically, one adjusts Δ so that on average A is roughly 0.5 (i.e., 50% acceptance). The above is a valid choice for use in the MRRTT algorithm, and one obtains correct averages of observables from it. Its major drawback, that becomes worse as M is increased, is that the random walk diffuses through configuration space very slowly.[4] This is because the harmonic force constant between adjacent beads goes as M/λ_T^2. The largest displacement one can achieve for a single bead is roughly $\lambda_T/\sqrt{M}$ and so for large M configurations of the path are very correlated during the walk. The autocorrelation time of observables can be so long that it is often difficult to obtain meaningful averages with "reasonable" expenditure of computing time. Since the harmonic forces of the free-particle propagator, rather than the hard-sphere interaction, are evidently the determining factor in the diffusion through configuration space, we have developed a random walk that takes the free-particle piece into account as much as possible. The *a priori* transition probability we use is based on the "normal modes" of the free-particle part of the density matrix

$$\frac{1}{2}\sum_{k}\sum_{\alpha=1}^{2}\frac{[\mathbf{q}_{i,\alpha}(k)]^2}{\sigma_k^2}\equiv\frac{1}{2}\frac{M}{\lambda_T^2}\sum_{l=1}^{M}[\mathbf{r}_i(l)-\mathbf{r}_i(l+1)]^2 \tag{30}$$

with

$$\frac{1}{\sigma_k^2}=\frac{8}{\lambda_T^2}\sin^2\left[\frac{\pi}{M}k\right] . \tag{31}$$

By definition, the normal-mode coordinates $\{\mathbf{q}\}$ are those that diagonalize the harmonic forces on the right-hand side of Eq. (30). They are

$$\mathbf{q}_{i,1}(k)=\sum_{l=1}^{M}\mathbf{r}_i(l)\cos\left[\frac{2\pi}{M}k(l-1)\right] , \tag{32}$$

and $\mathbf{q}_{i,2}(k)$ is obtained by replacing the cosine by sine in the above formula. The normal-mode index k lies in the range $1\le k\le(M-1)/2$ for M odd and $1\le k\le M/2$ for M even [when M is even and $k=M/2$ there is no $\alpha=2$ mode and the right-hand side of Eq. (31) must be reduced by a factor of 2]. One may extend the definition in Eq. (32) to $k=0$ in which case the mode corresponds to the center of mass of the path.

The *a priori* transition matrices used in this work can be summarized by the following separate types of transitions for each particle's path.

(1) Choose a trial position for the center of mass of the path $q'(0)$ uniformly in a cube of side length Δ centered about the initial center of mass. Compute A [Eq. (29)] and accept the new position with this probability.

(2) For each $k\le k^*$, in turn, choose a trial value for the normal-mode coordinate $q'(k)$ uniformly on the segment $[q(k)-\gamma\sigma_k, q(k)+\gamma\sigma_k]$, compute A and accept the new position with this probability.

(3) For all modes with $k>k^*$, *simultaneously* sample trial values $q'(k)$ out of Gaussian distributions with zero mean and width $\sigma_k(\langle[q'(k)]^2\rangle=\sigma_k^2)$. Compute and accept with probability A.

Steps 1, 2, and 3 are repeated for each particle's path in turn. For the most part, the parameters Δ, γ, and k^* are adjusted so that each of the three types of moves have an acceptance probability around 50% (γ may be chosen differently for each k). At *very* low densities or high temperatures when the interpolymer interaction is weak the acceptance of type (3) moves approaches 100% since in these cases the probability distribution of the normal modes closely resembles the Gaussian that is sampled. Moves of type (1) are the analog of the standard Monte Carlo moves of classical solids and fluids;[22] since the free-particle piece of the density matrix is held fixed only the interpolymer interaction comes into play. We developed moves of type (2) and (3) with the free-particle density matrix in mind along with the observation that the low-k modes (low frequency or long wavelength) make up the bulk of the size of a given path. The higher-k modes make up the "fine detail" of the path. The low-k modes will thus have a stronger interpolymer coupling than the high-k modes. This feature may be seen explicitly by observing how far the points on a path are displaced when one changes $q(k)$ by σ_k. The maximum displacement in this case is $\lambda_T/[M\sin(\pi k/M)]$, which is roughly λ_T/π for $k=1$ and λ_T/M for $k=M/2$. Furthermore, as k approaches $M/2$ the normal modes become increasingly oscillatory, and so there is a substantial amount of cancellation in the coupling of the mode to other polymers. The same ideas have been exploited in the method of "partial averaging" by Doll, Coalson, and Freeman[23] to include in an approximate way the effect of *all* Fourier components beyond the maximum one used in the simulation. The very weak coupling between the high-k modes and other paths enables us to sample a *set* of them simultaneously from the ideal gas propagator and still get a reasonable acceptance. As one lowers the temperature or increases the density it is clear that the coupling increases. In these cases the set of modes is broken up into several groups so that the acceptance for a group never falls below 20%. For a system of particles interacting with a realistic He-He pair potential (see Sec. V), we are experimenting with Monte Carlo moves in which displacements of type (2) are biased[24] in the direction of the generalized force conjugate to $q(k)$, and for displacements of type (3) trial values $q'(k)$ are sampled from slightly narrower Gaussians than those described above to account approximately for the interpolymer interaction (that tends to confine each polymer to a smaller region of space). The Monte Carlo moves mentioned in this paragraph leave averages unchanged since their use still gives rise to paths sampled from $\mathcal{P}(\mathcal{R})$. Nevertheless, we have found them to be extremely useful in that they significantly decrease the autocorrelation of observables and so one generates more reliable data for fixed number of passes through the system.[25]

C. Free-energy estimation

The conditions for two phases to coexist are equal temperatures, pressures, and chemical potentials. These constraints can be satisfied by the standard Maxwell double-tangent construction of the Helmholtz free energy. Therefore, to implement this technique one must be able to compute the free energy of both phases. As in classical simulations, it is difficult to estimate the free energy directly at a given density and temperature by Monte Carlo. While "mechanical" properties such as the energy and pressure are relatively straightforward to compute, "thermal" properties such as the entropy S ($F=E-TS$) tend to be rather troublesome, although some progress has been made.[26] The difficulty apparently stems from having to numerically estimate the partition function Z that is the *normalization constant* of the probability distribution the MRRTT algorithm samples.

In the fluid phase we have simply integrated the equation of state from low density,

$$f(\rho)=f_{\rm id}(\rho)+k_BT\int_0^{\rho}\frac{d\rho'}{\rho'}\left[\frac{P(\rho')}{\rho' k_BT}-1\right] , \tag{33}$$

where the ideal gas free-energy per particle is given by

$$f_{\rm id}(\rho)=k_BT[\ln(\rho\lambda_T^3)+\tfrac{3}{2}\ln 2\pi-1] . \tag{34}$$

The pressure was fit to a polynomial of degree 6 constrained to agree with the quantum mechanical virial ex-

pansion[27] to order ρ^2.

To compute the free energy in the solid phase we apply the thermodynamic integration technique of Frenkel and Ladd[28] to the PIMC simulation of quantum hard spheres. In this method a term is added to the Boltzmann factor that enables one to continuously transform the system into an Einstein crystal. Let

$$Z(\lambda)=\int d\mathcal{R}\, e^{-U_{\rm eff}(\mathcal{R})-\lambda r^2(\mathcal{R})}, \qquad f(\lambda)=-\frac{k_B T}{N}\ln Z(\lambda), \tag{35}$$

where

$$r^2(\mathcal{R})=\frac{1}{M}\sum_{l=1}^{M}\sum_{i=1}^{N}[\mathbf{r}_i(l)-\mathbf{r}_i^{(0)}]^2, \tag{36}$$

and $\mathbf{r}_i^{(0)}$ is the lattice position of the ith particle. The situation where $\lambda=0$ corresponds to the system of interest, whereas for large enough λ the system is accurately described by an Einstein crystal because each path is tightly bound to its lattice site. The derivative of the free energy per particle with respect to λ is given by

$$\frac{\partial f}{\partial\lambda}(\lambda)=\frac{k_B T}{N}\langle r^2(\mathcal{R})\rangle_\lambda . \tag{37}$$

The brackets $\langle\ \rangle_\lambda$ indicate an average in the ensemble using the integrand of Eq. (35) as its probability distribution. Thus the free energy $f(0)$ of the system is given by

$$f(0)=f(\lambda_{\rm max})-\frac{k_B T}{N}\int_0^{\lambda_{\rm max}} d\lambda\langle r^2(\mathcal{R})\rangle_\lambda . \tag{38}$$

The value of $\lambda_{\rm max}$ is chosen so that the system is nearly an Einstein crystal, where one has exact expressions for the free energy. It turns out that as λ is increased the interpolymer hard-sphere interaction becomes unimportant long before the "intrapolymer" piece from the free-particle density matrix does. Therefore, in practice $\lambda_{\rm max}$ is chosen so that the interparticle interaction term is a small perturbation and $f(\lambda_{\rm max})$ is very nearly the free energy of the harmonic system given by the Einstein term together with the free-particle density matrix. The small difference between $f(\lambda_{\rm max})$ and the free energy of the purely harmonic system is estimated by umbrella sampling.[22] This is achieved by directly sampling the harmonic portion of Eq. (35) and averaging the remaining factor.

IV. RESULTS

In this section we present our results for the thermodynamical, structural, and elastic properties of the quantum hard-sphere system along with the location of the melting-freezing transition. All quantities are reported in reduced units where the hard-sphere diameter σ is taken as the unit of length and $(\hbar^2/m\sigma^2)$ as the unit of energy. A convenient feature of the hard-sphere system is that for a given (reduced) temperature and density, the mass appears only through the reduction factor. In other words, the results at a Monte Carlo data point (ρ,T) may be applied to *any* hard-sphere system (characterized by m and σ). For pair potentials with an additional energy scale ϵ (see Sec. V) the de Boer parameter $\Lambda=(\hbar^2/m\sigma^2\varepsilon)$ must be taken as a third independent variable in the simulations. The results presented below are computed for systems with 108 particles, although some runs were performed with $N=256$, 500, and 864 to test for finite-size corrections. No statistically significant size dependence is observed in the energy and pressure. The initial configuration is usually a perfect fcc crystal (with all the steps of one particle's path situated on a lattice site). At low and moderate densities each particle quickly diffuses away from its lattice site while at higher densities the system remains a solid. To obtain results in the high-density fluid the random walk is started from an appropriately scaled configuration taken from a previous fluid run at lower density.

A. Equation of state and structure

The Monte Carlo data for the solid and fluid phases were taken along three isotherms of reduced temperature:[29] $T=1.6$, 4.0, and 8.0. Using the mass of the ^{4}He atom and effective helium diameter of 2.2 Å (see Sec. V) one finds that $(\hbar^2/m\sigma^2)$ is nearly 2.5 K, so the isotherms correspond to 4.0, 10.0, and 20.0 K for ^{4}He. To find the corresponding values for ^{3}He, multiply these temperatures by 1.37 (essentially the ratio of isotopic masses).

Tables I, II, and III contain the raw Monte Carlo data for the energy per particle and the pressure at various points in the (ρ,T) plane. By "raw data" we mean the simulation data for the system with M time slices: these values are used to extrapolate to the $M\to\infty$ limit. In the tables, n is the number of passes for each run (in thousands) where a pass is defined as an attempted random move for every one of the $3NM$ degrees of freedom (via the three types of moves described in Sec. III B). In practice several hundred passes at the beginning of the run were discarded to allow the system to equilibrate to the probability distribution $\mathcal{P}(\mathcal{R})$, except in some situations where 1000–4000 passes were discarded to insure equilibration. The uncertainties are the usual block estimates of the standard error.[22] At $T=1.6$ with $M=20$, we can generate 8000 passes per hour in the fluid phase at $\rho=0.2$ (using the moves of Sec. III B with $k^*=2$ and the rest of the modes moved simultaneously) and 6000 passes per hour in the solid phase at $\rho=0.38$ (with $k^*=4$ and the rest of the modes broken up into two groups) on a Cray X-MP computer.

One can see that most of the computational effort is concentrated in the high-density fluid. It is here where we found the longest autocorrelation times in the simulations. At the highest densities in the fluid a question of convergence remains since we observe relatively large ($\sim$1–2 %) fluctuations over long times ($\sim$5000 passes) in this region. We will see in the following subsection that these densities are fortunately above the thermodynamically determined freezing density and are thus metastable. It is possible that the system is attempting to phase separate in these runs, but it is also likely that the highly compressed fluid is very sluggish and so the autocorrelation of observables is much increased. In any event, the

error estimates at the points $(\rho,T)=(0.38,1.6)$, (0.45,4.0), and (0.57,8.0) should be viewed with some skepticism, although the energy and pressure do not appear to be significantly inconsistent with the more reliable results at the lower densities. This behavior is not unlike that of classical systems in the metastable fluid. We have performed simulations of the classical Lennard-Jones system in the metastable region at reduced temperature 2.74 and have found autocorrelation times similar to those in our quantum simulations of the metastable fluid.

The quantities ΔE and ΔP in Tables I, II, and III are the differences between the β-derivative and "Laplacian" estimators (see Sec. III A) of the energy and pressure, respectively. As the discretization M is increased these differences should go to zero, and, as may be seen in the tables, the Monte Carlo estimates for ΔE and ΔP decrease as M becomes larger. The smallness of these differences is a useful test of convergence, although not an absolute one. At low densities (roughly less than one-third of the freezing density) the behavior of ΔE and ΔP provided the only reliable measure of convergence, whereas at higher densities it is evident that there is a correction term with a slower M dependence that cancels out in the difference between β-derivative and Laplacian estimators. For the most part, ΔE and ΔP go as $M^{-3/2}$ for large M. This dependence may be argued heuristically from the functional form of the estimators for the differences, and is seen in the work of Ref. 15 for the two hard-sphere pair-distribution function. For most of the densities studied there is a contribution to the energy and pressure that vanishes more slowly than $M^{-3/2}$. The bulk of the data set is best fit by a M^{-1} correction term ($M^{-1/2}$ and $M^{-3/2}$ were tried and rejected), and so this form is used in all extrapolations. A test of this procedure may be obtained by comparing our extrapolated $M=\infty$ energies with those obtained at $T=0$ by GFMC in Ref. 3. Using the Debye theory, it will be shown in Sec. IV C that for nearly all densities studied here in the solid phase at $T=1.6$ and the highest densities at $T=4.0$ and 8.0 the system is, to within statistical error, in its ground state. At these points, the computed energy agrees with that from Ref. 3 to within the statistical error

TABLE I. Finite time-slice energy and pressure data in the fluid and solid phases along the $T=1.6$ isotherm.

ρ	M	E	ΔE	P	ΔP	n
			Fluid			
0.015	10	2.56±0.02	0.0025	0.0279±0.0002	0.000 03	8.4
0.03	10	2.72±0.025	0.0074	0.0645±0.0005	0.000 15	4.8
0.05	10	2.93±0.02	0.013	0.1292±0.0009	0.000 45	4.8
	20	2.92±0.025	0.0041	0.1288±0.0009	0.000 14	4.8
0.10	20	3.76±0.03	0.012	0.422 ±0.0025	0.000 82	4.8
0.15	20	5.12±0.02	0.023	1.031 ±0.004	0.0023	9.0
0.2063	10	7.47±0.04	0.113	2.41 ±0.010	0.0156	4.2
	20	7.35±0.02	0.049	2.39 ±0.006	0.0067	7.8
	40	7.30±0.03	0.017	2.375 ±0.008	0.0024	10.2
	80	7.31±0.05	0.005	2.38 ±0.013	0.0007	5.4
0.25	20	9.65±0.015	0.083	4.175 ±0.008	0.0138	20.4
	40	9.56±0.025	0.032	4.155 ±0.012	0.0053	12.3
0.30	20	13.09±0.025	0.146	7.43 ±0.015	0.029	15.6
	40	13.02±0.03	0.061	7.42 ±0.016	0.012	10.8
0.35	20	17.39±0.025	0.237	12.47 ±0.03	0.055	14.4
	40	17.18±0.03	0.112	12.33 ±0.03	0.026	54.0
0.38	20	20.32±0.03	0.319	16.54 ±0.08	0.081	21.6
	40	20.33±0.04	0.158	16.64 ±0.06	0.040	14.4
			Solid			
0.32	40	13.87±0.07	0.082	8.25 ±0.04	0.018	3.6
	80	13.82±0.10	0.027	8.32 ±0.04	0.0056	3.6
0.34	40	15.44±0.06	0.107	10.02 ±0.04	0.024	3.0
	80	15.42±0.08	0.037	10.06 ±0.05	0.009	3.0
0.3768	10	19.43±0.07	0.697	14.77 ±0.06	0.175	3.0
	20	19.09±0.05	0.437	14.50 ±0.04	0.110	6.0
	40	18.80±0.03	0.171	14.30 ±0.03	0.043	9.0
	80	18.63±0.04	0.056	14.15 ±0.04	0.015	6.0
0.42	40	23.41±0.06	0.285	21.16 ±0.08	0.079	3.0
	80	23.37±0.08	0.098	21.09 ±0.06	0.027	3.0
0.46	20	29.53±0.04	1.03	30.88 ±0.04	0.317	9.0
	40	28.95±0.04	0.46	30.22 ±0.05	0.140	6.0
	80	28.65±0.09	0.16	29.74 ±0.12	0.049	3.0

($\approx 1\%$). This is a fairly stringent test because the GFMC algorithm makes no short time or small τ approximation and so its results have no extrapolation errors. However, since GFMC is an iterative process it may still be subject to error due to lack of convergence.

Tables IV, V, and VI contain the extrapolated values for the energy, pressure, and free energy for the three temperatures studied. The free energies are obtained by the thermodynamic integration techniques discussed in the previous section. In the solid phase we compute the free-energy at one density ρ_0 for each isotherm using the method of Ref. 28, and then use the expression

$$f(\rho)=f(\rho_0)+\int_{\rho_0}^{\rho} d\rho' \frac{P(\rho')}{(\rho')^2} \tag{39}$$

to obtain f at other densities. The values of $f(\rho_0)$ may be found in Table VII.

At low density the equations of state in Tables IV, V, and VI go over to the ideal gas values, namely, $\rho k_B T$, $\frac{3}{2}k_B T$, and Eq. (34) for the pressure, energy, and free energy, respectively. Furthermore, the low-density Monte Carlo data for P and E agree within its statistical error with the second virial expressions for these quantities. Therefore, our Monte Carlo data provide the hard-sphere fluid equation of state all the way from the imperfect gas regime up to the solidification density.

In the solid phase the entropy, $S=(E-F)/T$, decreases to zero with increasing density. This result can be interpreted in terms of the elementary excitation picture of quantum solids, where the excited states are long-wavelength phonons. The expressions for the thermal properties in terms of the phonon spectrum are well known.[30,31] We will show below that this phonon description is qualitatively correct for nearly all the densities studied here in the solid. We only note in passing that as the density increases the amount of thermal excitation must diminish because the solid becomes more "stiff" to the excitation of longitudinal and transverse phonons. Thus for fixed temperature, as the density increases the solid goes into its ground state. This behavior is seen clearly in Tables IV, V, and VI. In the cases where comparison may be made, the energy matches onto the $T=0$ values of Ref. 3. The equality of E and F at high density is a strong test of the correctness of the free energy computed by transforming the system into an Einstein crystal as well as of the convergence to the $M\to\infty$ limit. The "energy" of the system is computed by two different methods; the β-derivative (or the Laplacian) kinetic energy estimator and the thermodynamic integration implied by Eqs. (38) and (39), and they are found to agree.

TABLE II. Same as in Table I except $T=4.0$.

ρ	M	E	ΔE	P	ΔP	n
			Fluid			
0.02	10	6.27±0.06	0.0032	0.0909±0.0008	0.000 04	3.6
0.04	10	6.54±0.06	0.0069	0.207 ±0.0016	0.000 18	4.8
0.07	10	6.90±0.07	0.0127	0.431 ±0.0034	0.000 59	4.8
0.13	10	8.16±0.07	0.0302	1.190 ±0.0060	0.0026	4.8
0.20	10	10.30±0.07	0.059	2.92 ±0.015	0.0079	4.8
0.26	10	13.13±0.05	0.11	5.72 ±0.02	0.018	9.6
	20	13.14±0.07	0.039	5.72 ±0.02	0.0067	9.6
0.32	10	17.20±0.08	0.16	10.56 ±0.07	0.034	4.8
	20	17.06±0.05	0.068	10.49 ±0.04	0.015	9.6
	40	16.88±0.08	0.020	10.54 ±0.04	0.005	7.2
0.38	10	22.49±0.04	0.24	18.52 ±0.04	0.061	14.4
	20	22.34±0.08	0.13	18.39 ±0.09	0.033	9.6
	40	22.33±0.09	0.047	18.22 ±0.08	0.014	7.2
0.42	10	27.08±0.04	0.35	26.22 ±0.06	0.093	14.4
	20	26.85±0.04	0.21	26.04 ±0.05	0.053	33.6
	40	26.90±0.23	0.077	26.36 ±0.25	0.021	3.6
0.45	10	30.90±0.08	0.41	33.56 ±0.11	0.122	19.2
	20	30.89±0.06	0.26	33.72 ±0.09	0.078	14.4
	40	30.60±0.12	0.11	33.35 ±0.33	0.030	7.2
			Solid			
0.43	20	25.73±0.13	0.23	24.19 ±0.12	0.067	4.8
	40	25.37±0.13	0.078	24.05 ±0.12	0.022	4.8
0.46	20	29.39±0.09	0.33	30.81 ±0.09	0.10	4.8
	40	29.27±0.15	0.11	30.43 ±0.12	0.035	4.8
0.48	20	32.35±0.10	0.42	36.36 ±0.11	0.13	4.8
	40	31.89±0.10	0.15	35.91 ±0.09	0.046	9.6
0.51	20	37.01±0.11	0.60	46.07 ±0.14	0.20	4.8
	40	36.66±0.15	0.20	45.63 ±0.14	0.069	4.8

The uncertainty estimates of the energy and pressure in Tables IV, V, and VI are obtained by taking the standard errors of the finite M data (from Tables I, II, and III) and using the usual formulas for the propagation of errors in the linear extrapolation process. The error estimates of the Helmholtz free energy are computed by the following "synthetic-data" method.[32] In both the fluid and solid phases the pressure is fit to a polynomial in the density by the least-squares method. These polynomials are next integrated via Eqs. (33) or (39) to obtain the free energy $f(\rho)$. One may compute a rough estimate of the uncertainty in $f(\rho)$ by repeating the above least-squares fit and integration not with the original pressure data $\{P_i\}$, but rather with synthetic data $\{P_i+\sigma_i\eta_i\}$, where σ_i is the standard error of P_i and η_i is a random deviate sampled from a Gaussian distribution with zero mean and unit variance. Typically, several hundred such synthetic data are generated and the resulting variance in $f(\rho)$ is a measure of its error.[33] The same technique is used to compute the error estimates in Table VII where the corresponding integral is Eq. (38) and the fitting function is a polynomial in $1/(c+\lambda)$ and c is an additional fitting parameter.[28]

In order to put the computed equations of state in a convenient form, we provide the coefficients of the fitting polynomials mentioned in the preceding paragraph. The pressure P and the energy per particle E/N are fit to the following functional forms for each isotherm:

$$
\begin{aligned}
P(\text{solid}) &= \sum_{l=0}^{3} a_l(\rho-\bar{\rho})^l , \\
P(\text{fluid}) &= \rho k_B T\left[1+b_2\rho+\sum_{l=3}^{6} b_l\rho^{l-1}\right] , \\
\frac{E}{N}(\text{solid}) &= \sum_{l=0}^{3} A_l(\rho-\bar{\rho})^l , \\
\frac{E}{N}(\text{fluid}) &= \tfrac{3}{2}k_B T(1+\tfrac{1}{3}B_2\rho)+\sum_{l=3}^{6} B_l\rho^{l-1} .
\end{aligned}
\tag{40}
$$

The values of the coefficients a_l, b_l, A_l, B_l, and $\bar{\rho}$ may be found in Table VIII. Except for $\bar{\rho}$ and the second virial coefficients, b_2 and B_2 (obtained from Ref. 27), the coefficients in the table are determined by fitting the PIMC data. Because the values b_l and B_l with $l \geq 3$ have been used to fit the entire range of the fluid phase, they should not be interpreted as estimates for the actual coefficients of the virial expansions of the pressure and kinetic energy. Rather, they are simply the parameters of a smooth function that fits our Monte Carlo data within its error bars. As the fitting functions rapidly become unreliable when the density is taken outside the region of the simulation data, it is suggested that the functions only be used in the range indicated by Tables IV, V, and VI. The integration of the pressure as in Eqs. (33) and (39)

TABLE III. Same as in Table I except $T=8.0$.

ρ	M	E	ΔE	P	ΔP	n
			Fluid			
0.025	6	12.39±0.15	0.0080	0.226±0.003	0.000 14	4.8
0.05	6	12.71±0.11	0.016	0.505±0.004	0.000 55	4.8
0.09	6	13.38±0.09	0.035	1.104±0.007	0.0021	4.8
	12	13.35±0.13	0.010	1.100±0.009	0.0007	4.8
0.16	10	15.31±0.12	0.029	2.83 ±0.02	0.0032	4.8
0.25	10	18.90±0.13	0.063	7.13 ±0.04	0.0105	4.8
0.32	10	22.91±0.08	0.107	13.53 ±0.05	0.023	9.6
0.39	10	28.82±0.17	0.17	24.5 ±0.15	0.044	4.8
0.43	10	33.56±0.13	0.23	33.8 ±0.14	0.065	4.8
0.46	10	37.24±0.11	0.29	42.5 ±0.15	0.088	19.2
	20	37.35±0.13	0.13	42.4 ±0.17	0.041	19.2
0.50	10	43.58±0.12	0.39	57.9 ±0.2	0.129	24.0
	20	43.47±0.22	0.20	57.9 ±0.3	0.069	9.6
0.54	10	51.24±0.14	0.50	78.6 ±0.4	0.18	28.8
	20	51.22±0.21	0.29	78.7 ±0.7	0.10	28.8
0.57	10	57.92±0.13	0.61	98.5 ±0.3	0.23	19.2
	20	57.76±0.16	0.39	98.3 ±0.7	0.15	19.2
			Solid			
0.53	20	43.06±0.22	0.27	58.0 ±0.3	0.096	4.8
	40	42.95±0.15	0.09	57.3 ±0.2	0.031	9.6
0.56	20	48.14±0.14	0.37	71.9 ±0.3	0.139	4.8
	40	47.78±0.19	0.12	70.9 ±0.3	0.046	4.8
0.59	20	54.81±0.17	0.58	89.2 ±0.3	0.21	4.8
	40	54.36±0.17	0.17	88.6 ±0.3	0.069	9.6
0.65	20	71.88±0.14	1.04	142.3 ±0.3	0.45	4.8
	40	70.92±0.13	0.36	140.1 ±0.3	0.16	9.6

TABLE IV. Energy, pressure, and free energy (E, P, and f, respectively) for the hard-sphere system at temperature $T=1.6$. The hard-sphere diameter σ is the unit of length and $\hbar^2/m\sigma^2$ is the unit of energy. The first column is the number density. The data above the line are results from the fluid phase, and below the line from the solid.

ρ	E	P	f
0.015	2.56±0.02	0.0279±0.0002	−4.757±0.001
0.03	2.72±0.03	0.0644±0.0005	−3.396±0.004
0.05	2.91±0.05	0.1285±0.002	−2.207±0.009
0.10	3.76±0.03	0.4220±0.003	0.04 ±0.02
0.15	5.11±0.02	1.029 ±0.004	2.22 ±0.03
0.2063	7.26±0.03	2.368 ±0.008	5.05 ±0.03
0.25	9.49±0.05	4.14 ±0.025	7.70 ±0.03
0.30	12.97±0.06	7.41 ±0.035	11.39 ±0.03
0.35	16.97±0.07	12.19 ±0.07	15.95 ±0.04
0.38	20.34±0.09	16.75 ±0.15	19.17 ±0.05
0.32	13.8 ±0.2	8.4 ±0.1	13.45 ±0.2
0.34	15.4 ±0.17	10.1 ±0.1	15.15 ±0.2
0.3768	18.57±0.03	14.1 ±0.03	18.55 ±0.2
0.42	23.4 ±0.2	21.0 ±0.15	23.25 ±0.2
0.46	28.43±0.07	29.5 ±0.10	28.4 ±0.2

yields analytic expressions for the free energy in the fluid and solid phases, respectively.

The two curves in Fig. 1 are our results for the pair-distribution function $g(r)$ at representative densities in the solid and fluid at $T=1.6$. The points are the $T=0$ hard-sphere values from Ref. 3 at the same densities. In both cases the agreement is quite good, although the systematic difference in the solid phase is not yet understood. The discrepancy is evidently too large to be explained by thermal fluctuations at $T>0$ that tend to reduce the structure in the correlation function. In the solid the only excitations are phonons that in a finite system give rise to a thermal energy roughly proportional to T^4. In the fluid of *distinguishable* particles, however, there are many free-particle-like excitations that lead to a thermal energy proportional to T. As seen in Ref. 4, $g(r)$ in the fluid is nonetheless quite insensitive to temperature in this region and may be successfully compared to $T=0$ results.

In Fig. 2 we compare our solid and fluid hard-sphere pair-distribution functions to those determined at $T=0$ in Ref. 34 for ^{4}He using a realistic helium pair potential. The choice of the hard-sphere diameter is the same as in the perturbation theory to be discussed in Sec. V. In this theory the perturbative reference system is determined by matching the hard-sphere diameter to the scattering length of the repulsive part of the pair potential. Although this prescription involves two-body information only, the comparison in Fig. 2 indicates that the mapping is accurate even at high densities where many-body correlations are important. The agreement between these pair-distribution functions strongly suggests the validity of the hard-sphere perturbation theory to be used in Sec. V.

TABLE V. Same as in Table IV except $T=4.0$.

ρ	E	P	f
0.02	6.26±0.06	0.0909±0.0008	−16.323±0.003
0.04	6.53±0.06	0.206 ±0.0016	−13.018±0.009
0.07	6.89±0.07	0.431 ±0.003	−9.90 ±0.02
0.13	8.15±0.07	1.189 ±0.006	−5.32 ±0.04
0.20	10.27±0.07	2.915 ±0.015	−0.38 ±0.05
0.26	13.2 ±0.14	5.72 ±0.05	4.31 ±0.05
0.32	16.85±0.1	10.51 ±0.05	9.86 ±0.06
0.38	22.25±0.1	18.15 ±0.09	16.68 ±0.07
0.42	26.60±0.1	25.9 ±0.1	22.14 ±0.07
0.45	30.65±0.1	33.8 ±0.2	26.83 ±0.08
0.43	25.0 ±0.3	23.9 ±0.3	24.25 ±0.1
0.46	29.2±0.3	30.1 ±0.3	28.3 ±0.1
0.48	31.5±0.2	35.5 ±0.2	31.3 ±0.1
0.51	36.4±0.3	45.2 ±0.3	36.2 ±0.1

TABLE VI. Same as in Table IV except $T=8.0$.

ρ	E	P	f
0.025	12.4 ±0.15	0.226±0.003	−39.217±0.006
0.05	12.7 ±0.1	0.505±0.004	−32.65 ±0.02
0.09	13.3 ±0.3	1.10 ±0.02	−26.15 ±0.05
0.16	15.3 ±0.1	2.83 ±0.02	−17.8 ±0.10
0.25	18.9 ±0.1	7.13 ±0.04	−7.9 ±0.14
0.32	22.85±0.08	13.52 ±0.05	0.7 ±0.14
0.39	28.7 ±0.2	24.4 ±0.15	10.9 ±0.14
0.43	33.4 ±0.15	33.7 ±0.15	17.7 ±0.15
0.46	37.5 ±0.3	42.3 ±0.4	23.5 ±0.15
0.50	43.4 ±0.5	57.9 ±0.6	32.1 ±0.2
0.54	51.2 ±0.5	78.8 ±1.5	42.1 ±0.2
0.57	57.5 ±0.4	98.1 ±1.5	50.7 ±0.2
0.53	42.9 ±0.4	56.7 ±0.5	38.9 ±0.2
0.56	47.5 ±0.4	70.0 ±0.6	45.2 ±0.2
0.59	54.0 ±0.4	88.0 ±0.6	52.4 ±0.2
0.65	70.1 ±0.3	137.9 ±0.7	69.7 ±0.2

Table IX provides a solid and fluid pair-correlation function for each isotherm. In this study we have computed $g(r)$ at 45 points in the (ρ,T) plane for various values of M. We are presently preparing these functions for availability via electronic mail or other means.

B. Melting-freezing transition

The Monte Carlo calculation of the free energy enables one to locate the thermodynamic phase transition between the solid and fluid phases by the Maxwell double tangent construction. The resulting coexisting densities ρ_f and ρ_s, pressure P_m, and fractional density change $(\rho_s-\rho_f)/\rho_s$, appear in Table X. The errors in these quantities are computed by the synthetic data method elaborated on above. The coexisting densities increase with increasing temperature; varying from the $T=0$ values near $\rho=0.27$ toward the classical values near $\rho=1.0$. Similarly, the fractional change in density is seen to increase toward the classical value of 0.094. The melting pressure P_m increases, of course, because the two-phase region moves to higher density. Figs. 3(a), 3(b), and 3(c) display the simulation data for the pressure in the two phases as a function of density. The coexistence region is indicated by a horizontal line at the melting pressure.

The hard-sphere solid-fluid phase transition is interesting because in the classical regime the total energy is $(3/2)k_BT$ and so the energy difference between the two phases $\Delta E=E_s-E_f$ vanishes, while the entropy (per particle) difference $\Delta S=S_s-S_f=-1.16k_B$ does not.[2] At $T=0$, on the other hand, ΔS is zero by the third law and $\Delta E\sim 1.2$.[3] Therefore, the transition is purely entropic at high temperature and purely energetic at $T=0$. The ΔE here should not be confused with the same symbol used in Sec. IV A. Table XI contains ΔE and the latent heat $L=-T\Delta S$ for the isotherms of this work and the $T=0$ results of Ref. 3. From the table one can see that the latent heat of fusion approaches the classical hard-sphere value from below with increasing temperature. Evidently

TABLE VII. Free energy per particle f at temperature T and density ρ_0 computed by the thermodynamic integration technique that transforms the system into an Einstein crystal.

T	ρ_0	f
1.6	0.34	15.1 ±0.2
4.0	0.43	24.25±0.1
8.0	0.53	38.9 ±0.2

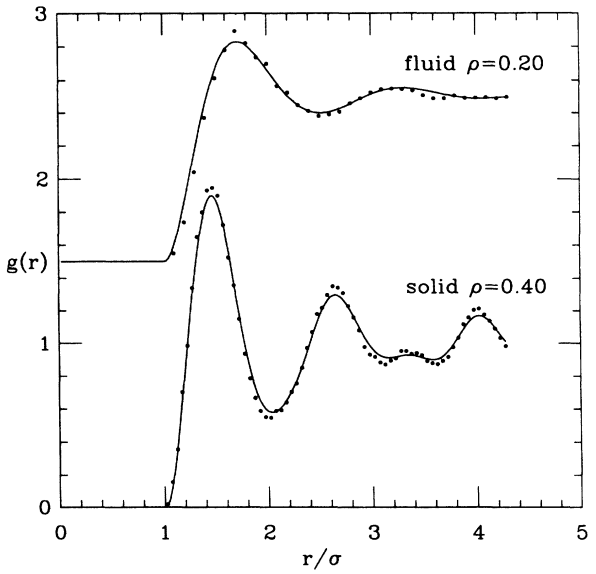

FIG. 1. Pair-distribution functions of the quantum hard-sphere system in the fluid and solid phases. The circles are the results of Ref. 3 computed at $T=0$ by GFMC. The solid lines are the PIMC results of this work at $T=1.6$ The fluid data are shifted up by 1.5. r/σ is the pair separation divided by the hard-sphere diameter.

the crossover to a purely entropic transition occurs at a lower temperature than those studied in this paper since our ΔE is zero within the statistical error. This result is somewhat surprising because the system is far from the classical regime (the coexisting solid is still very close to its ground state). At these temperatures nearly all of the entropy resides in the coexisting fluid, except at the highest isotherm where the solid's entropy reaches 30% of the fluid's entropy. Using the hard-sphere mapping onto ^{4}He at the temperatures 4, 10, and 20 K mentioned above, our results of $-\Delta S/k_B = 0.67$, 0.87, and 0.98 compare favorably with the experimentally measured values of Grilly and Mills[35] that are 0.69, 0.81, and 0.88, respectively. The ^{4}He experimental results indicate that ΔS goes to zero *very* rapidly below about 3 K, whereas above this temperature the dependence is fairly small. It is quite possible that the same mechanism that takes ΔS to zero very quickly in ^{4}He causes an equally rapid cross-

TABLE VIII. Polynomial fitting coefficients for the thermodynamic functions. The first column indicates the reduced temperature at which the fit is made. The top two sections contain the coefficients for the pressure and energy per particle in the solid and fluid phases of the hard-sphere system [see Eq. (40)]. The bottom two sections contain the coefficients for the free energy in the solid and fluid phases of ^{3}He and ^{4}He computed by the perturbation theory of Sec. V [see Eq. (65)].

Hard-sphere pressure

T	$\bar{\rho}$	a_0	a_1	a_2	a_3
1.6	0.341	1.011 543e +1	9.179 291e +1	5.354 980e +2	5.291 513e +2
4.0	0.46	3.011 766e +1	2.428 155e +2	1.190 265e +3	
8.0	0.56	6.999 369e +1	5.218 706e +2	2.589 526e +3	

T	b_2	b_3	b_4	b_5	b_6
1.6	9.3173	4.748 849e +1	2.243 319e +2	1.133 930e +2	1.278 039e +2
4.0	5.9794	2.015 351e +1	7.027 258e +1	1.992 319e +1	1.976 852e +2
8.0	4.6061	1.146 099e +1	4.175 994e +1	−2.036 726e +1	1.410 626e +2

Hard-sphere energy

T	$\bar{\rho}$	A_0	A_1	A_2	A_3
1.6	0.341	1.537 828e +1	7.882 443e +1	3.024 776e +2	−3.621 555e +2
4.0	0.46	2.885 257e +1	1.337 482e +2	3.096 735e +2	
8.0	0.56	4.768 538e +1	1.840 619e +2	7.261 958e +2	

T	B_2	B_3	B_4	B_5	B_6
1.6	10.225	2.866 135e +1	3.342 756e +2	−7.390 349e +2	9.684 652e +2
4.0	5.0355	3.925 610e +1	5.126 965e +1	2.023 030e +2	−4.549 980e +1
8.0	3.0730	5.754 747e +1	−1.056 026e +2	5.025 265e +2	−2.269 225e +2

^{3}He free energy

T	$\bar{\rho}$	c_0	c_1	c_2	c_3
1.6	0.341	1.917 247e +0	3.581 421e +1	1.506 804e +2	5.126 445e +2
4.0	0.46	9.074 765e +0	9.527 020e +1	3.176 667e +2	
8.0	0.56	2.153 975e +1	1.835 558e +2	5.636 364e +2	

T	d_1	d_2	d_3	d_4	d_5
1.6	−1.874 896e +0	−6.054 717e +1	2.473 671e +2	−9.273 062e +1	2.062 746e +2
4.0	4.487 117e +0	−5.780 431e +1	3.089 573e +2	−3.650 207e +2	5.002 176e +2
8.0	1.730 043e +1	−6.340 031e +1	3.770 909e +2	−4.421 434e +2	4.947 304e +2

^{4}He free energy

T	$\bar{\rho}$	c_0	c_1	c_2	c_3
1.6	0.341	−1.840 057e +0	1.993 071e +1	1.389 877e +2	5.620 179e +2
4.0	0.46	3.351 235e +0	7.855 647e +1	3.210 000e +2	
8.0	0.56	1.421 756e +1	1.682 361e +2	5.785 354e +2	

T	d_1	d_2	d_3	d_4	d_5
1.6	−6.669 998e +0	−8.019 329e +1	2.375 545e +2	−3.914 038e +1	1.670 411e +2
4.0	−1.888 019e +0	−6.861 202e +1	2.817 800e +2	−2.986 434e +2	4.613 137e +2
8.0	9.972 807e +0	−7.456 250e +1	3.744 508e +2	−4.410 566e +2	5.079 694e +2

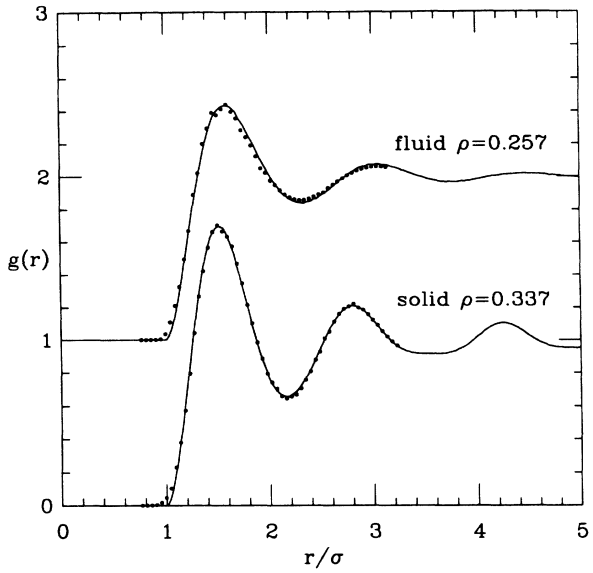

FIG. 2. Pair distribution functions of quantum systems in the fluid and solid phases. The circles are the $T=0$ results of Ref. 34 for the helium pair potential. The solid lines are the hard-sphere results of this work at $T=2.0$. The fluid data are shifted up by 1.0. The choice of hard-sphere diameter σ is that described in Secs. IV and V.

over from the $\Delta S\neq 0$, $\Delta E=0$ regime to the $\Delta S=0, \Delta E\neq 0$ regime in the Bose quantum hard-sphere system.

Lindemann's ratio γ is the root-mean-square-deviation of a particle from its lattice position divided by the nearest-neighbor distance d,[36]

$$\gamma=\frac{1}{d}\left\langle\frac{1}{N}\sum_{i=1}^{N}(\mathbf{r}_i-\mathbf{r}_i^{(0)})^2\right\rangle^{1/2}. \tag{41}$$

As in classical simulations, there is a technical problem in that particles may exchange among lattice sites during the course of the simulation. There is nothing physically wrong with this diffusion; it merely complicates the computation of γ since it is not always clear to which lattice site a particle belongs. In practice this did not turn out to be a problem because the exchange is very infrequent and was not observed in our simulations. To take care of the slow drift of the system's center of mass, after each pass the starting fcc lattice is shifted by the amount the center of mass of all NM monomers has diffused during the pass. Table XII contains our values of γ for the hard-sphere solid.

The quantity γ has long been a tool for measuring a solid's proximity to melting. Lindemann's "law" is that when γ reaches a critical value γ_m the system melts. The belief is that γ_m should be nearly independent of temperature and roughly the same for different pair potentials (provided that they have a repulsive core). Both experiment and Monte Carlo simulation[5] have shown that this melting law is fairly accurate for simple *classical* systems (e.g., argon, xenon, and sodium) where γ_m is approximately 0.15 (for classical hard spheres $\gamma_m=0.13$). In quantum solids such as helium the light mass of the particles gives rise to a very large zero-point motion in which each particle pushes out against its cage of neighbors thereby stabilizing the solid to much lower densities than would be allowed classically. For example, the classical hard-sphere system melts at $\rho=1.04$, whereas quantum mechanically at $T=0$ it melts near $\rho=0.27$. Ground-state studies[37–39] have shown that at these lower densities where quantum melting takes place the Lindemann ratio is much increased. For the Lennard-Jones model of ^{4}He at $T=0$ in Ref. 37 Lindemann's ratio at melting is $\gamma_m=0.27$. The last line of Table XII contains γ interpolated at the melting densities. As expected, there is evidently a smooth transition between the classical and $T=0$ values of 0.13 and ~ 0.27, respectively.

We note that γ may have a large number dependence

TABLE IX. Pair-distribution function $g(r)$ in the fluid (f) and solid (s) phases.

r/σ	$T=1.6$ (f) $\rho=0.30$	1.6 (s) 0.3768	4.0 (f) 0.38	4.0 (s) 0.46	8.0 (f) 0.46	8.0 (s) 0.56
1.000	0.0000	0.0000	0.0000	0.0000	0.0000	0.0000
1.025	0.0050	0.0064	0.0084	0.0096	0.0142	0.0164
1.050	0.0342	0.0417	0.0559	0.0647	0.0921	0.1073
1.075	0.0866	0.1094	0.1436	0.1657	0.2382	0.2775
1.100	0.1625	0.2040	0.2636	0.3076	0.4286	0.5069
1.125	0.2535	0.3176	0.4079	0.4791	0.6551	0.7783
1.150	0.3554	0.4503	0.5635	0.6713	0.8872	1.0777
1.175	0.4686	0.5911	0.7342	0.8752	1.1259	1.3779
1.200	0.5826	0.7378	0.9005	1.0818	1.3462	1.6652
1.225	0.7029	0.8911	1.0590	1.2857	1.5360	1.9273
1.250	0.8159	1.0421	1.2075	1.4701	1.6958	2.1429
1.275	0.9316	1.1801	1.3470	1.6432	1.8176	2.3091
1.300	1.0380	1.3129	1.4639	1.7940	1.9001	2.4124
1.325	1.1364	1.4352	1.5596	1.9088	1.9452	2.4572
1.350	1.2259	1.5444	1.6369	2.0007	1.9520	2.4363
1.375	1.3036	1.6301	1.6935	2.0559	1.9337	2.3604
1.400	1.3694	1.7051	1.7269	2.0770	1.8865	2.2396
1.425	1.4284	1.7593	1.7416	2.0702	1.8131	2.0777

TABLE IX. (*Continued*).

r/σ	$T=1.6$ (f) $\rho=0.30$	1.6 (s) 0.3768	4.0 (f) 0.38	4.0 (s) 0.46	8.0 (f) 0.46	8.0 (s) 0.56
1.450	1.4751	1.7969	1.7365	2.0302	1.7332	1.8882
1.475	1.5057	1.8133	1.7178	1.9683	1.6427	1.6855
1.500	1.5297	1.8160	1.6814	1.8842	1.5480	1.4787
1.525	1.5423	1.7966	1.6393	1.7815	1.4505	1.2753
1.550	1.5454	1.7657	1.5855	1.6637	1.3550	1.0877
1.575	1.5384	1.7230	1.5229	1.5405	1.2628	0.9185
1.600	1.5247	1.6663	1.4595	1.4113	1.1762	0.7739
1.625	1.5004	1.5971	1.3913	1.2844	1.0980	0.6571
1.650	1.4731	1.5269	1.3231	1.1591	1.0271	0.5656
1.675	1.4431	1.4473	1.2565	1.0423	0.9623	0.5017
1.700	1.4057	1.3625	1.1899	0.9354	0.9028	0.4612
1.725	1.3660	1.2779	1.1255	0.8418	0.8514	0.4419
1.750	1.3232	1.1970	1.0649	0.7601	0.8080	0.4412
1.775	1.2818	1.1137	1.0106	0.6910	0.7745	0.4532
1.800	1.2386	1.0359	0.9620	0.6366	0.7433	0.4747
1.825	1.1918	0.9635	0.9133	0.5933	0.7225	0.5002
1.850	1.1470	0.8970	0.8738	0.5644	0.7033	0.5261
1.875	1.1073	0.8351	0.8345	0.5442	0.6885	0.5506
1.900	1.0646	0.7810	0.8063	0.5346	0.6792	0.5722
1.925	1.0240	0.7362	0.7800	0.5325	0.6784	0.5899
1.950	0.9880	0.6969	0.7556	0.5351	0.6787	0.6036
1.975	0.9541	0.6642	0.7410	0.5426	0.6825	0.6155
2.000	0.9207	0.6392	0.7280	0.5555	0.6921	0.6281
2.025	0.8929	0.6215	0.7207	0.5710	0.7066	0.6469
2.050	0.8668	0.6094	0.7171	0.5889	0.7224	0.6734
2.075	0.8431	0.6058	0.7178	0.6114	0.7433	0.7097
2.100	0.8253	0.6055	0.7202	0.6367	0.7647	0.7608
2.125	0.8090	0.6091	0.7284	0.6639	0.7915	0.8260
2.150	0.7942	0.6182	0.7388	0.6985	0.8188	0.9066
2.175	0.7847	0.6338	0.7535	0.7355	0.8495	0.9980
2.200	0.7789	0.6522	0.7696	0.7770	0.8804	1.0972
2.225	0.7758	0.6748	0.7891	0.8266	0.9113	1.2002
2.250	0.7749	0.7017	0.8112	0.8790	0.9451	1.2978
2.275	0.7762	0.7293	0.8345	0.9366	0.9789	1.3858
2.300	0.7804	0.7638	0.8579	0.9968	1.0107	1.4560
2.325	0.7887	0.7974	0.8834	1.0568	1.0423	1.5048
2.350	0.7987	0.8356	0.9114	1.1180	1.0741	1.5306
2.375	0.8098	0.8740	0.9360	1.1749	1.1003	1.5319
2.400	0.8239	0.9160	0.9629	1.2288	1.1281	1.5087
2.425	0.8401	0.9584	0.9889	1.2757	1.1511	1.4641
2.450	0.8547	0.9997	1.0140	1.3136	1.1704	1.4024
2.475	0.8719	1.0408	1.0384	1.3426	1.1862	1.3327
2.500	0.8919	1.0815	1.0610	1.3586	1.1966	1.2541
2.525	0.9110	1.1188	1.0823	1.3648	1.2028	1.1747
2.550	0.9320	1.1544	1.0994	1.3600	1.2066	1.1009
2.575	0.9518	1.1821	1.1178	1.3457	1.2037	1.0339
2.600	0.9705	1.2088	1.1306	1.3201	1.1967	0.9756
2.625	0.9904	1.2306	1.1419	1.2908	1.1882	0.9269
2.650	1.0097	1.2460	1.1510	1.2514	1.1746	0.8897
2.675	1.0254	1.2548	1.1592	1.2104	1.1588	0.8624
2.700	1.0453	1.2605	1.1609	1.1661	1.1413	0.8429
2.725	1.0611	1.2587	1.1616	1.1223	1.1214	0.8333
2.750	1.0731	1.2516	1.1606	1.0785	1.0999	0.8293
2.775	1.0837	1.2405	1.1557	1.0386	1.0785	0.8323
2.800	1.0949	1.2240	1.1501	1.0009	1.0564	0.8418
2.825	1.1051	1.2049	1.1401	0.9703	1.0325	0.8559
2.850	1.1123	1.1817	1.1296	0.9416	1.0108	0.8746
2.875	1.1175	1.1574	1.1158	0.9208	0.9908	
2.900	1.1206	1.1324	1.1025	0.9048	0.9711	

TABLE IX. (*Continued*).

r/σ	$T=1.6$ (f) $\rho=0.30$	1.6 (s) 0.3768	4.0 (f) 0.38	4.0 (s) 0.46	8.0 (f) 0.46	8.0 (s) 0.56
2.925	1.1225	1.1052	1.0891	0.8929	0.9527	
2.950	1.1231	1.0799	1.0745	0.8880	0.9370	
2.975	1.1213	1.0520	1.0573	0.8873	0.9236	
3.000	1.1177	1.0287	1.0409	0.8891	0.9083	
3.025	1.1142	1.0063	1.0232	0.8942	0.8985	
3.050	1.1076	0.9877	1.0068	0.9025	0.8908	
3.075	1.1010	0.9704	0.9919	0.9113	0.8846	
3.100	1.0925	0.9552	0.9775			
3.125	1.0834	0.9427	0.9634			

that has not been extensively studied in this work. The slow convergence to the $N\rightarrow\infty$ limit is due to a large contribution from long-wavelength phonons that give a correction term proportional to $N^{-1/3}$ for classical systems and quantum systems at $T>0$. At $T=0$ the correction goes as $N^{-2/3}$. In both cases it can be shown that the finite system's γ is less than that of the infinite system. Assuming the data is in the $N^{-1/3}$ regime, a test at $\rho=0.3768$, $T=1.6$ with $N=108$ and 256 indicates the Lindemann's ratio for the 108 particle system underestimates the infinite system result by about 7% [$\gamma(108)=0.214$ while $\gamma(\infty)=0.23$]. This value could be an overestimate of the actual extrapolation because at low temperature there may be a large region where γ has a correction term that behaves more like $N^{-2/3}$ before finally crossing over to $N^{-1/3}$. Using the finite system Debye theory discussed in the next subsection, we find that near melting (along the three isotherms) 108 particles is accurately in the $N^{-1/3}$ regime and the amount of extrapolation (5–8 %) is comparable to the above test at $\rho=0.3768$. For the point $\rho=0.53, T=2.0$, well above the melting density, the Debye theory suggests that the crossover to the $N^{-1/3}$ regime does not occur until $N\sim10\,000$ and there is a total extrapolation of about 3.5%. In the classical hard-sphere system near melting the $N^{-1/3}$ dependence of γ has been observed using Monte Carlo and indicates that an 108 particle system is about 16% below the thermodynamic limit.[40]

It may be possible to generalize Lindemann's melting law to all temperatures. The idea is that the values of γ_m as a function of the melting temperature T_m for the quantum hard-sphere system will form a "universal" curve that is applicable for all simple systems possessing a melting-freezing transition. The only difficulty in applying this generalization to other quantum systems is in appropriately scaling the temperature variable. We conjecture that a reasonable prescription is given by the choice of hard-sphere reference system used in the perturbative study of ^{3}He and ^{4}He discussed in Sec. V. In the perturbation theory an effective hard-sphere diameter σ^* is chosen as the s-wave scattering length of the repulsive part of the pair potential of interest. For both classical and quantum systems it is believed that the melting-freezing phenomenon is essentially determined by the repulsive core of the interaction and other details (such as an attractive well) are of secondary importance. Given that the above choice of hard-sphere reference system provides a good description of the phase transition in ^{3}He and ^{4}He at finite temperatures (see Sec. V), it is reasonable to suppose that one may use this mapping in the generalization of Lindemann's law as well. Specifically, let σ^* be the s-wave scattering length of the pair potential as defined above, then define T^* by

$$T^*=\frac{k_BT}{\left[\dfrac{\hbar^2}{m(\sigma^*)^2}\right]}\ . \tag{42}$$

We claim that the system will melt when γ reaches $\gamma_m(T^*)$, with γ_m determined from the *hard-sphere* data at reduced temperature T^*. This formulation agrees with the classical and $T=0$ forms[39] of Lindemann's law since at large T^* γ_m goes over to the classical result of $\gamma_m=0.13$ and as $T^*\rightarrow0$ it evidently approaches $\gamma_m=0.27$. The test of this law in the intermediate temperature regime would require extensive determinations of the phase transition in a variety of quantum systems (such as the helium isotopes, the one-component plas-

TABLE X. Parameters of the hard-sphere melting-freezing transition. All quantities are reported in the reduced units of the text. The solid and fluid densities are ρ_s and ρ_f, respectively. $\Delta\rho/\rho_s$ is the fractional change in density $(\rho_s-\rho_f)/\rho_s$. The coexistence pressure is P_m.

T	ρ_s	ρ_f	P_m	$\Delta\rho/\rho_s$
1.6	0.360±0.017	0.348±0.016	12.2±2.0	0.034 ±0.004
4.0	0.465±0.005	0.442±0.005	31.3±1.3	0.0495±0.002
8.0	0.537±0.005	0.503±0.005	59.5±2.0	0.063 ±0.003

ma,[41] and Yukawa nuclear matter systems discussed in Ref. 39) at finite temperatures. Furthermore, additional hard-sphere data of increased accuracy for a wider range of T^* along with careful extrapolation to the $N \rightarrow \infty$ limit is required to better describe the universal curve $\gamma_m(T^*)$. Such a computational project is feasible at present although it is not clear that it is warranted theoretically. Refinements in the method of choosing T^* are certainly possible, although it would probably be difficult to decide among different choices [it should be noted that even among purely classical systems the γ_m of Lindemann's law is "violated" roughly by 15% (Ref. 5)]. Finally, we note that the effect of Bose and Fermi statistics on Lindemann's law at low temperatures is largely unexplored.[42] It would be interesting to compare the melting-freezing transition of ^{3}He to that of a fictitious mass-3 boson system interacting with the same pair potential.[43] Since the effect of statistics should be negligible in the solid, any differences (say in the value of γ_m) are solely due to the relative stability of the Bose and Fermi *fluids* near freezing. The Fermi fluid would be less stable since its free energy is higher than the Bose. Although the differences may be small, the universal curve $\gamma_m(T^*)$ should depend on the statistics the particles obey. We call attention to the above point to note that any such difference is not addressed in this study where Boltzmann

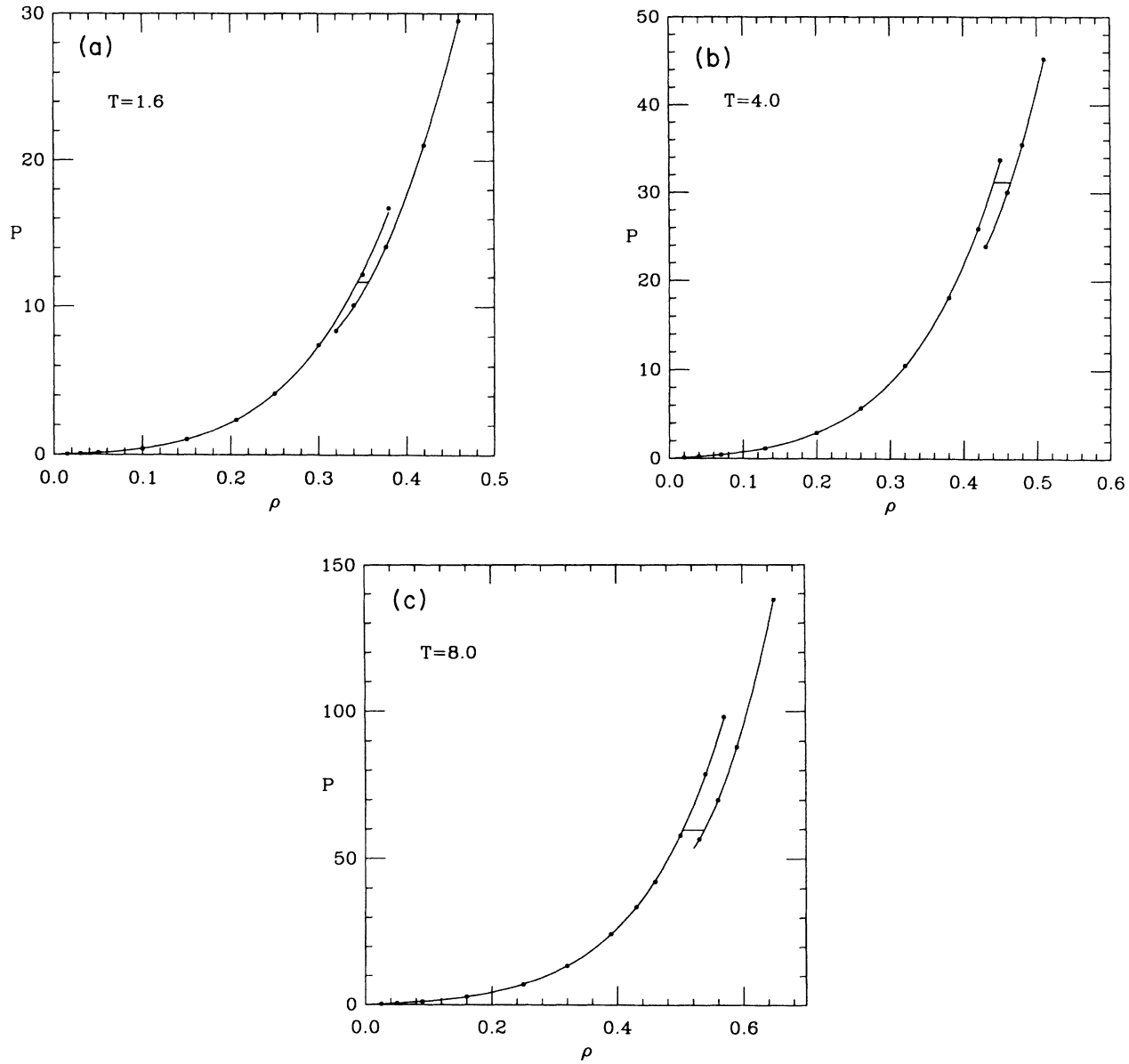

FIG. 3. (a) Pressure P vs density ρ for the fluid and solid phases of the hard-sphere system along the $T=1.6$ isotherm. The units for pressure, temperature, and density are $\hbar^2/m\sigma^5$, $\hbar^2/m\sigma^2$, and σ^{-3}, respectively. The circles are the path-integral Monte Carlo data. The solid curves are the least-squares-fitting functions discussed in the text. The horizontal line denotes the thermodynamically determined coexistence region between fluid and solid. (b) The same as in (a) except along the $T=4.0$ isotherm. (c) The same as in (a) except along the $T=8.0$ isotherm.

TABLE XI. Differences between the coexisting solid and fluid phases. The energy difference is defined by $\Delta E = E_s - E_f$ and the entropy difference by $\Delta S = S_s - S_f$. Both are per particle quantities. The latent heat of fusion for the quantum system is $L = -T\Delta S$ and $-T\Delta S_{\rm cl}$ is the corresponding value of the classical system at the same temperature (from Ref. 2). The $T=0$ point is estimated from the result of Ref. 3.

T	ΔE	$-T\Delta S$	$-T\Delta S_{\rm cl}$
0.0	1.2±0.4	0.0	0.0
1.6	0.1±0.2	1.1±0.25	1.9
4.0	0.0±0.3	3.5±0.35	4.6
8.0	−0.3±0.6	7.9±0.7	9.3

statistics are assumed, although we believe that the effect should only be seen at temperatures lower than those investigated here.

C. Elastic properties of the solid phase

The elastic constants of the hard-sphere solid at low temperatures are computed here to explore the validity of the Debye theory, to test the consistency of the free-energy computations of Sec. IV A, and to provide exact Monte Carlo results for the elastic moduli of a quantum solid. Previously the computation of the elastic properties of quantum solids has been limited to approximate theories and variational studies.[44]

The elasticity theory for the system studied in this paper applies only to very long wavelength phonons. The discontinuous nature of the hard-sphere interaction and the large zero-point motion preclude the validity of the standard harmonic theory[30,44] that involves a Taylor series expansion in the displacement from the perfect crystal lattice. The strong zero-point repulsion between particles provides the "restoring force" to long-wavelength acoustic distortions. The elastic moduli computed in this work provide a quantitative measure of the system's stiffness to these distortions.

To define the elastic constants, let $\mathbf{u}(\mathbf{x})$ be the displacement field of a deformed crystal. The strain tensor is defined by

$$\eta_{ij} = \frac{1}{2}\left[\frac{\partial u_i}{\partial x_j} + \frac{\partial u_j}{\partial x_i} + \frac{\partial u_k}{\partial x_i}\frac{\partial u_k}{\partial x_j}\right], \tag{43}$$

where i and j take on the values 1, 2, or 3 and the repeated index k is summed over. Let $f(\eta)$ and $f(0)$ denote the free energies per particle of the deformed and undeformed crystals, respectively. The elastic constants C_{ijkl} are defined by the following expansion about the undeformed state:

$$\rho f(\eta) = \rho f(0) + T_{ij}\eta_{ij} + \tfrac{1}{2}C_{ijkl}\eta_{ij}\eta_{kl} + \cdots , \tag{44}$$

where all repeated indices are summed over. T_{ij} is the stress tensor. We shall use the standard Voigt notation: $C_{11}=C_{1111}$, $C_{12}=C_{1122}$, $C_{44}=C_{1212}$, etc. For crystals with cubic symmetric (such as the fcc) there are only three independent elastic constants that may be taken as C_{11}, C_{12}, and C_{44}. Wallace[45] discusses the above expansion and symmetry properties in detail.

As in Ref. 46, to estimate the elastic moduli a small strain, parametrized by ε, is applied to the simulation cell. During the simulation in this deformed cell the stress tensor is measured and the resulting linear dependence of it on ε is used to extract the $C_{\alpha\beta}$. We have used two types of strain that correspond to the following shear transformations of the simulation cell:

$$x' = x + \varepsilon_1 y, \quad x' = (1-\varepsilon_2)x ,$$
$$y' = y, \quad y' = (1+\varepsilon_2)y ,$$
$$z' = z, \quad z' = z .$$

The following relationships[46] are used to determine the elastic constants:

$$\mu_1 = \frac{\rho}{\varepsilon_1}\frac{\partial f}{\partial \varepsilon_1} = (C_{44} - P) + O(\varepsilon_1^2) , \tag{45a}$$

$$\mu_2 = \frac{\rho}{\varepsilon_2}\frac{\partial f}{\partial \varepsilon_2} = 2(C_{11} - C_{12} - P) + O(\varepsilon_2^2) , \tag{45b}$$

$$\rho\left[\frac{\partial P}{\partial \rho}\right]_T = \tfrac{1}{3}(C_{11} + 2C_{12} + P) . \tag{45c}$$

The inverse isothermal compressibility on the left-hand side of Eq. (45c) is estimated by performing simulations at densities $\rho \pm \Delta\rho$ and finite differencing the pressure with $\Delta\rho \sim 0.015$. The quantities $\partial f/\partial\varepsilon_1$ and $\partial f/\partial\varepsilon_2$ are computed in a manner analogous to the pressure in Eq. (24) and the discussion following it. In this case the derivative of $U_{\rm eff}$ with respect to ε_ν provides an estimator for $\partial f/\partial\varepsilon_\nu$.

TABLE XII. Lindemann's ratio γ (rms deviation from lattice site divided by the nearest-neighbor distance) for the densities and temperatures (ρ, T) in the solid phase. The last line contains the deduced value of γ at melting for each isotherm.

$T=1.6$		$T=4.0$		$T=8.0$	
ρ	γ	ρ	γ	ρ	γ
0.32	0.225±0.003	0.43	0.204±0.001	0.53	0.168±0.001
0.34	0.236±0.001	0.46	0.183±0.001	0.56	0.154±0.002
0.3768	0.214±0.001	0.48	0.175±0.001	0.59	0.142±0.001
0.42	0.195±0.001	0.51	0.164±0.001	0.65	0.125±0.001
0.46	0.181±0.001				
ρ_m	0.225±0.010	ρ_m	0.181±0.003	ρ_m	0.165±0.003

We compute the elastic constants at the reduced densities 0.34, 0.43, and 0.53. In these computations we attempt to take the temperature low enough so that quantum solid is very close to its ground state. In this way we may use the resulting $C_{\alpha\beta}$ in the Debye theory to estimate the amount of thermal excitation above the ground state at the three isotherms studied in this work. An important test can be made by comparing the thermal excitation in the free energies of Table VII to that predicted by the Debye model. We will see below that the Debye theory qualitatively predicts the magnitude of the excitation, although the temperature is too high (it is near melting) to yield precise results. The results of our Monte Carlo determination of the energy, pressure, $(\partial P/\partial\rho)$, μ_1, and μ_2 at the three densities appear in Table XIII. The relative errors in $(\partial P/\partial\rho)$, μ_1, and μ_2 are larger than those for E and P because second derivatives of the free energy are more difficult to estimate by Monte Carlo than are first derivatives.

From the quantities in Table XIII one may compute the elastic constants, the Debye temperature, propagation speeds, and Poisson's ratio. These quantities are in Table XIV. We define Poisson's ratio ν to be minus the ratio of the strain along y to the strain along x when the stress is incremented in the x direction:

$$\nu=-\frac{\eta_{yy}}{\eta_{xx}}, \quad =\frac{C_{12}+P}{C_{11}+C_{12}}, \quad \delta T_{xx}\neq 0 . \tag{46}$$

Poisson's ratio actually depends on the orientation for an anisotropic crystal, but we will consider only the above quantity in this paper. For an isotropic system $-1\leq\nu\leq\frac{1}{2}$. If ν is less than zero the system contracts along y when compressed along x, thus most systems in nature have $\nu>0$. For quantum hard spheres we find Poisson's ratio is 0.48 at low density $\rho=0.34$ and decreases to 0.41 at $\rho=0.53$. These values of ν may be compared to results for the classical hard-sphere system[46,47] where ν is 0.34 at the melting density $\rho=1.04$ and evidently decreases linearly to 0.2 at close packing $\rho=1.41$.

To define the remaining quantities in the table, we note from Wallace that the propagation velocities $c_s(\hat{\mathbf{k}})$ of an acoustic wave traveling in the $\hat{\mathbf{k}}$ direction are related to the eigenvalues of the following equation:

$$m\rho c^2(\hat{\mathbf{k}})\hat{\mathbf{e}}_i=A_{ijkl}\hat{\mathbf{k}}_j\hat{\mathbf{k}}_l\hat{\mathbf{e}}_k , \tag{47}$$

where repeated indices are summed over, $m\rho c^2$ is the eigenvalue, $\hat{\mathbf{e}}_i$ is the ith component of the eigenvector $\hat{\mathbf{e}}$ (also known as the polarization vector because it is the direction along which the displacement field oscillates), and the tensor A is

$$A_{ijkl}=T_{jl}\delta_{ik}+C_{ijkl} . \tag{48}$$

Equation (47) is a 3×3 symmetric matrix eigenvalue equation, so for each direction $\hat{\mathbf{k}}$ there are three mutually orthogonal polarization vectors $\hat{\mathbf{e}}(\hat{\mathbf{k}},s)$ $s=1,2,3$ with corresponding propagation velocities $c_s(\hat{\mathbf{k}})$. The Debye theory result of low-temperature crystals[30] is that the thermal energy of a large system is given by

$$E(T)\approx E(0)+N\frac{3\pi^4}{5}k_BT\left[\frac{T}{\Theta_D}\right]^3 , \tag{49}$$

where

$$(k_B\Theta_D)^{-3}\equiv\frac{1}{18\pi^4\rho\hbar^3}\left\langle\sum_{s=1}^{3}[c_s(\hat{\mathbf{k}})]^{-3}\right\rangle \tag{50}$$

with the brackets $\langle\ \rangle$ denoting an angular average over directions $\hat{\mathbf{k}}$. The angular average is performed here by a simple Monte Carlo method in which roughly 5000 random directions are sampled. For each direction the matrix in Eq. (47) is diagonalized and the resulting sum of inverse cubes of the propagation velocities is averaged to provide an estimate of the right-hand side of Eq. (50). As expected for a crystal with high symmetry, we find it is approximately true that the eigensolutions of Eq. (47) breakup into a longitudinal mode with $\hat{\mathbf{e}}$ nearly parallel to $\hat{\mathbf{k}}$ and two nearly degenerate transverse modes with $\hat{\mathbf{e}}$ perpendicular to $\hat{\mathbf{k}}$. This is exactly true in an isotropic system. The longitudinal mode has a speed of propagation larger than that of the transverse modes because the former modulates the density in space whereas the latter produce "shear" distortions that keep the density constant. The zero-point repulsion between particles thus provides a stronger restoring force to longitudinal phonons than to transverse phonons. In light of these ideas, we define $\bar{c}_l$ to be the angular average of the largest propagation velocity and $\bar{c}_t$ to be the average of the two smaller ones. These "longitudinal" and "transverse" speeds and Θ_D appear in Table XIV for the three densities studied.

TABLE XIII. Monte Carlo data for the elastic study at three density and temperature points (ρ,T). E, P, $\rho(\partial P/\partial\rho)$ are the energy per particle, pressure, and isothermal compressibility. μ_1 and μ_2 are the curvatures of the free energy with respect to strain as defined in the text. The energy, pressure, and compressibility data for $T=1.6$ are actually computed from a fit to the $T=0$ data of Kalos in Ref. 3.

ρ	T	E	P	$\rho\left[\frac{\partial P}{\partial\rho}\right]$	μ_1	μ_2
0.34	1.6	15.36±0.1	9.91±0.1	36.4±1.0	11.6±0.3	25.2±0.5
0.43	2.5	24.45±0.1	22.85±0.1	87.0±1.0	41.5±0.5	87.0±1.0
0.53	4.0	39.9 ±0.3	53.2 ±0.2	234.0±6.0	128.6±1.3	296.0±2.0

TABLE XIV. Elastic properties of the hard-sphere solid at low temperature. The first two columns give the density and temperature. C_{11}, C_{12}, and C_{44} are the three independent elastic constants of the fcc crystal. Θ_D is the Debye temperature and $\bar{c}_l$ and $\bar{c}_t$ are the angularly averaged longitudinal and transverse sound velocities, respectively. Poisson's ratio is ν. All quantities are reported in the reduced units of the text.

ρ	T	C_{11}	C_{12}	C_{44}	Θ_D	$\bar{c}_l$	$\bar{c}_t$	ν
0.34	1.6	48.1±1.0	25.6±1.0	21.5±0.3	7.9	11.7	4.5	0.48
0.43	2.5	124.0±1.4	57.3±1.3	64.4±0.5	16.7	17.2	7.8	0.44
0.53	4.0	351.0±6.0	150.0±6.0	182.0±1.0	30.9	26.7	13.2	0.41

In Figs. 4 and 5 we compare our hard-sphere Debye temperatures to those obtained experimentally for solid ^{3}He and ^{4}He at low temperatures.[48] The mapping of the hard-sphere system onto the helium solids is the same one to be used below in the hard-sphere perturbation theory. From the figures, the hard-sphere Θ_D lies systematically below the experimental values although the density dependence is well reproduced. As mentioned above, the longitudinal phonons are more difficult to excite than transverse phonons because of the modulation in density that the former induce. Therefore, the Debye temperature is primarily a measure of the thermal contribution of *transverse* phonons (one may estimate that longitudinal excitations contribute less than 10% of Θ_D). The fact that the hard-sphere Θ_D is smaller than the values for the helium solids implies that the hard-sphere system offers *less* resistance to the formation of long-wavelength transverse phonons than helium does. This is a curious result because one might believe that the attractive part of the He-He pair potential would soften all phonon modes. We are presently performing PIMC simulations using an accurate He-He pair potential[49] and the high-temperature approximation of Ceperley and Pollock[17] to study both the equation of state and elastic properties of solid helium. We believe that this study will illuminate the source of the discrepancy in Θ_D between quantum hard spheres and real helium. The discrepancy may be due to (1) the inability of the hard-sphere reference system to describe accurately the transverse strain derivatives of the helium free energy, (2) the lack of an attractive well in the hard-sphere pair potential, (3) a deficiency in the He-He pair potential of Ref. 49, or (4) the fact that ^{4}He and ^{3}He form hcp crystals (at these densities), while the hard spheres studied here were fcc.

In their experimental study of solid helium, Sample and Swenson[48] observe that in the range of molar volumes from 11 to 19 cm^3 the ratio of ^{3}He to ^{4}He Debye temperatures is nearly constant with $\Theta_3/\Theta_4=1.18$. As mentioned by these authors, within the standard harmonic approximation[30] the tensor A on the right-hand side of Eq. (47) depends only on the number density ρ because A is related to strain derivatives of the potential energy $U=\sum_{i,j} v(r_{ij})$ evaluated at the perfect lattice configuration. The mass dependence of each sound velocity is thus $c \propto 1/\sqrt{m}$. Observing that $k_B\Theta_D \propto \rho^{1/3}\hbar c$ and that ^{3}He and ^{4}He have the same potential U yields

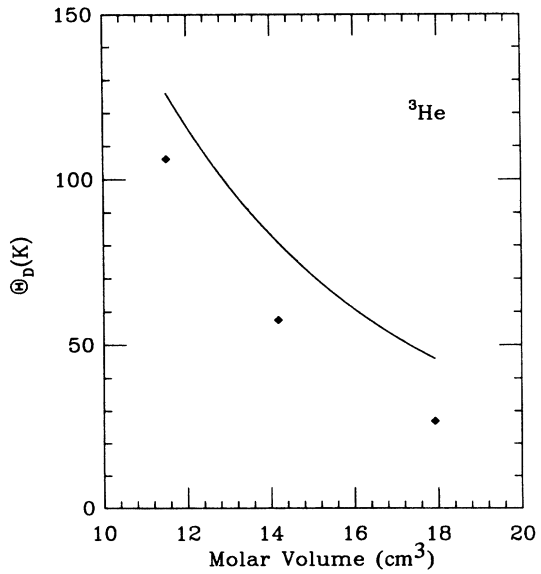

FIG. 4. Debye temperature Θ_D in K° for solid ^{3}He as a function of molar volume. The solid curve denotes the experimental values from Ref. 48. The diamonds are our zeroth-order hard-sphere perturbation-theory predictions for ^{3}He.

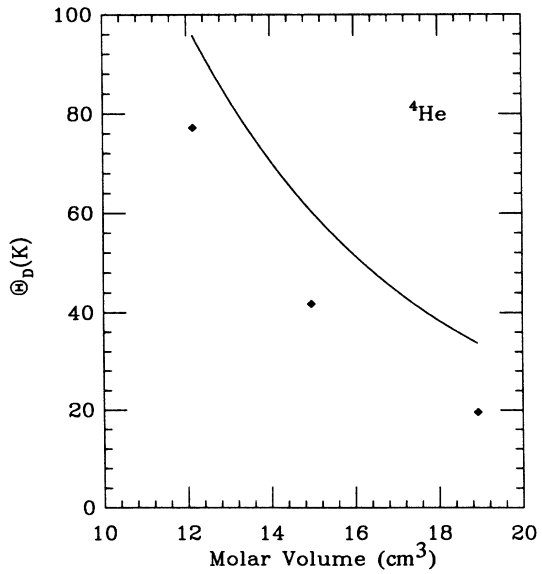

FIG. 5. Same as Fig. 4 except for ^{4}He.

$$\Theta_3/\Theta_4=(m_4/m_3)^{1/2}=1.152 ,$$

where m_3 and m_4 are the masses of the helium isotopes, and Θ_3 and Θ_4 are evaluated at the same number density. This prediction is quite close to the experimental ratio although the validity of the derivation is suspect because of the high degree of anharmonicity in solid helium. The standard harmonic theory applied to helium for the above range of volumes yields an unstable crystal (some of the c^2 are negative). As mentioned above, the large zero-point repulsion is what actually stabilizes the solid phase. Therefore, for solid helium we expect that A in Eq. (47) is strongly dependent on ρ, m, and $\hbar$. Note that for quantum solids A will contain a large contribution from the strain derivatives of the kinetic energy as well as from the potential energy. One may use the scaling properties with m of the hard-sphere system to compute the ratio Θ_3/Θ_4. This should be a good approach because, as we have seen, the hard-sphere system contains the large zero-point motion observed in solid helium. A simple, but unsuccessful, result may be obtained by assuming both ^{3}He and ^{4}He can be modeled by hard-sphere systems with the *same* diameter σ. Using the hard-sphere scaling one finds that

$$c_s(\hat{\mathbf{k}},\rho,m)=\frac{\hbar}{m\sigma}c_s^*(\hat{\mathbf{k}},\rho^*) \tag{51}$$

and

$$k_B\Theta_D(\rho,m)=\frac{\hbar^2}{m\sigma^2}\Theta_D^*(\rho^*) , \tag{52}$$

where the "asterisk" denotes a dimensionless quantity, for example $\rho^*=\rho\sigma^3$. This dependence on mass implies that $\Theta_3/\Theta_4=m_4/m_3=1.327$ and is in poor agreement with experiment. The defect with this model is that σ is not allowed to depend on the mass. In the scattering length model of helium used throughout this paper (to compute, for example, Θ_D in Figs. 4 and 5) the hard-sphere diameter does depend on the mass of the isotope. As will be seen in Sec. V, the ^{3}He effective diameter σ_3 is about 1.8% smaller than the ^{4}He value σ_4 because the lighter mass of the ^{3}He atom allows it to penetrate into the repulsive core slightly more than ^{4}He. We choose to include this mass dependence in the following simple manner. If one assumes a density-independent Grüneisen constant γ_0 over the range of interest then one has

$$\Theta_D^*(\rho^*)=\alpha_0(\rho^*)^{\gamma_0} . \tag{53}$$

The experimental data suggest that this is a fairly reasonable description of Θ_D. Use of Eq. (52) yields

$$\Theta_3/\Theta_4=\frac{m_4}{m_3}\left[\frac{\sigma_3}{\sigma_4}\right]^{3\gamma_0-2}=1.165 , \tag{54}$$

where we have used the value $\gamma_0=3.05\pm0.2$ that is from a least-squares fit to the Θ_D data in Table XIV.[50] This prediction is slightly better than the harmonic theory result of 1.152, but more importantly it follows from a model that has the correct zero-point motion of the quantum solid. Presumably, if the shape of the helium pair potential were different then the ratio σ_3/σ_4 would be changed and so would the value Θ_3/Θ_4. For example, if σ_3 were only 1% smaller than σ_4 then Θ_3/Θ_4 would be 1.235. Therefore, it is possible that the proximity of the experimental ratio to $(m_4/m_3)^{1/2}$ is entirely a coincidence.

Rather than use the infinite system result in Eq. (49) to evaluate the thermal contribution of phonons, one may easily compute this quantity for a finite system. In this way we may calculate the thermal excitation in the free energy of an 108 particle system and compare it to the Monte Carlo value computed by the thermodynamic integration in Eq. (38). To compute the thermal contribution one assumes that phonon states with excitation spectrum $\hbar\omega(\mathbf{k},s)$ are the excited states of the system, where $\mathbf{k}$ is a wave vector satisfying the Born–von Kármán boundary conditions of the periodic box. The excitation spectrum is next approximated as in the Debye scheme

$$\omega(\mathbf{k},s)=c_s(\hat{\mathbf{k}})k , \tag{55}$$

where $k=|\mathbf{k}|$. This expression is asymptotically exact as $k\rightarrow0$ for the infinite system. The free energy and energy of the system at temperature T within this approximation are given by

$$F(T)\approx E(0)+k_BT\sum_{\mathbf{k},s}\ln(1-e^{-\beta\hbar\omega(\mathbf{k},s)}) \tag{56a}$$

and

$$E(T)\approx E(0)+\sum_{\mathbf{k},s}\hbar\omega(\mathbf{k},s)(e^{\beta\hbar\omega(\mathbf{k},s)}-1)^{-1} , \tag{56b}$$

where we note that $F(0)=E(0)$ since $TS(T)$ vanishes as $T\rightarrow0$ for this system. The sum on $\mathbf{k}$ is over the Born–von Kármán wave vectors in the first Brillouin zone and s ranges over the three acoustic modes. Note that $E(0)$ is not the standard harmonic theory result given by the static lattice potential energy plus the sum of $\hbar\omega(\mathbf{k},s)/2$, but rather the total ground-state kinetic energy of the hard-sphere solid.[51] With this choice of $E(0)$, Eqs. (56) are asymptotically exact as $T\rightarrow0$ for a large system.

Table XV contains $\delta E\equiv E(T)-F(T)$ computed by both PIMC and the Debye theory. The quantity ΔE is convenient to consider because the $E(0)$ terms cancel out so that only finite-temperature data are required. At the low-temperature point, $T=1.6$, the thermal excitation δE is quite small—roughly the same size as the Monte Carlo error. At this temperature the PIMC and Debye model [$D(T)$ in Table XV] predictions for δE agree within large error bars. Thus, to within the statistical error, the thermodynamic integration to compute $F(T)$ is superfluous [$E(T)$ may be used to the same level of accuracy], but provides a useful consistency check of the methods used in this work. At the higher temperatures, $T=4.0$ and 8.0, δE is definitely nonzero and is approximately 3% and 9% of the total energy, respectively. $D(T/2)$ in Table XV is δE at temperature $T/2$ and demonstrates the rapid increase with temperature for the finite system [compare with Eq. (49) for the infinite system]. We also include the result for the infinite system,

TABLE XV. The difference $\delta E = E(T) - F(T)$ between energy and free energy at temperature T computed by various methods in the solid phase. The energy unit is $\hbar^2/m\sigma^2$. The first two columns are the density and temperature. PIMC is the value determined from Monte Carlo simulation for 108 particles. The last four columns are values computed within the Debye theory using the elastic constants of Table XIV. $D(T)$ is the Debye result for 108 particles at temperature T. $D(N=\infty)$ is the result at temperature T for the infinite system. D (disp) is the same as $D(T)$ except using a phonon spectrum with "simulated" dispersion. $D(T/2)$ is the same as $D(T)$ except at one-half the temperature.

ρ	T	PIMC	$D(T)$	$D(N=\infty)$	D (disp)	$D(T/2)$
0.34	1.6	0.32±0.26	0.25	0.27	0.40	0.018
0.43	4.0	0.8 ±0.3	0.95	1.08	1.6	0.055
0.53	8.0	4.0 ±0.5	2.4	2.7	4.0	0.14

$D(N=\infty)$, at temperature T to show the small effect of finite size. The prediction of the Debye theory estimates the size of δE reasonably well but the temperature is too high to give quantitative agreement. By this we mean that at these temperatures there is a significant contribution from phonons with wave vector $\mathbf{k}$ large enough so that the linear dispersion relation, Eq. (55), is no longer accurate. The effect may be estimated by putting in "artificial" dispersion and observing the resulting change it induces in the quantities. We model the dispersion by the replacement

$$\omega(\mathbf{k},s) \rightarrow \omega(\mathbf{k},s)\frac{\sin(ka_c)}{ka_c} , \tag{57}$$

where the "cutoff" distance a_c is chosen, somewhat arbitrarily, to be one quarter of the fcc conventional cell edge length. For this choice of a_c the argument of the sine function reaches $\pi/2$ just as $\mathbf{k}$ reaches the surface of the first Brillouin zone along the x, y, and z directions. Examination of the experimentally measured phonon dispersion relations in solid helium[44] reveals that this is a reasonable model of dispersion. As can be seen in Table XV, the thermal excitation depends strongly on the presence of dispersion: at the three points studied there is roughly a 60% increase in δE when the dispersion is added. From this observation we conclude that phonons near the zone boundary are significantly excited. This is not true at lower temperatures, roughly $< T/2$, where expressions (56) should be quite accurate. It is possible that the use of the unknown "correct" dispersion relation $\omega(\mathbf{k},s)$ will bring the δE computed within the phonon scheme into agreement with the PIMC results. However, given that wave vectors $\mathbf{k}$ near the zone boundary are excited (at least when the system is near melting), it is very likely that for these $\mathbf{k}$ the independent phonon approximation breaks down and there is a nonnegligible *anharmonic* contribution to δE. This contribution would be difficult to compute.

An interesting result is obtained if one computes the *total* energy E and Lindemann ratio γ within the harmonic theory using the spectra in Eqs. (55) and (57). In this approximation one has

$$E(T) \approx \sum_{\mathbf{k},s} \hbar\omega(\mathbf{k},s)[n(\mathbf{k},s)+\tfrac{1}{2}] , \tag{58}$$

$$\gamma^2(T) \approx \frac{1}{d^2}\frac{1}{N}\sum_{\mathbf{k},s}\frac{\hbar}{m\omega(\mathbf{k},s)}[n(\mathbf{k},s)+\tfrac{1}{2}] , \tag{59}$$

where

$$n(\mathbf{k},s) = (e^{\beta\hbar\omega(\mathbf{k},s)}-1)^{-1}$$

is the mean occupation number of mode $(\mathbf{k},s)$. The additional term $\frac{1}{2}$ added to $n(\mathbf{k},s)$ is the zero-point contribution of the harmonic oscillator. The more accurate treatment discussed above replaces this contribution with the exact values $E(0)$ and $\gamma^2(0)$ for the hard-sphere solid. From Table XVI one sees that the expressions (58) and (59) yield surprisingly good results given the apparent severity of making a harmonic approximation to the *full* Hamiltonian. For the total energy E the "linear" and "simulated dispersion" spectra give deviations from the exact PIMC result by 50% and 20%, respectively. The maximum discrepancy in γ is only 20% and is less than 10% for most points. It is reasonable that the energy is less accurate than γ because, as may be seen in Eq. (59), the latter weights the small k phonons more heavily. These long wavelength, small-k phonon degrees of freedom are more accurately described as independent simple harmonic oscillators than are the phonons near the zone

TABLE XVI. Comparison of the total energy E and Lindemann's ratio γ computed by Monte Carlo and the Debye theory. The density and temperature are ρ and T. All data are for 108 particles and are reported in the reduced units of the text. PIMC refers to the path integral Monte Carlo data. "Debye" is the Debye theory prediction and "Disp" is the Debye result using a phonon spectrum with simulated dispersion.

	ρ	T	E	γ
Debye	0.34	1.6	21.6	0.271
Disp			16.3	0.287
PIMC			15.4	0.236
Debye	0.43	4.0	37.9	0.209
Disp			28.9	0.222
PIMC			25.0	0.204
Debye	0.53	8.0	65.6	0.168
Disp			50.5	0.179
PIMC			42.9	0.168

boundary. In either case, it is remarkable that even semiquantitative agreement may be obtained with this very crude approximation.

The Debye model predictions of the thermal excitation δE suggest an alternate and more convenient way to compute the free energy in the solid. One may start at a density ρ_0 high enough so that $F(\rho_0)\approx E(\rho_0)$ ($\delta E\approx 0$) and perform simulations at lower densities as well, and finally integrate the pressure in Eq. (39) to obtain the free energy. This procedure is more convenient than that used here (the transformation to an Einstein crystal in Sec. III C) since it does not require an additional program to simulate the hard-sphere system with harmonic attraction to each lattice position [Eq. (35)]. This alternate procedure may not be more computationally efficient, however. As the density increases the number of time slices M must be increased to maintain accurate results, thereby increasing both the computer time per pass and the autocorrelation of observables. On the other hand, as the harmonic coupling constant λ is increased the quantum paths decouple from one another, the acceptance approaches 100%, and the autocorrelation becomes small. Which of the two methods is the more efficient depends on the circumstances (for example, the temperature) and degree of accuracy desired.

The elastic constant study performed here demonstrates that one may achieve at least semiquantitatively accurate results for the quantum hard-sphere solid within the Debye phonon theory. The computation of Θ_D for ^{3}He and ^{4}He using the hard-sphere elastic properties reach a similar level of accuracy. It should be noted that the quantitative Debye theory computations presented here required Monte Carlo simulation to determine the $C_{\alpha\beta}$.

V. PERTURBATIVE STUDY OF HELIUM

It is of interest to use the hard-sphere results to make predictions about actual systems in nature. In classical systems it has long been known[52] that a successful theory of Lennard-Jones systems results from "perturbing" about the hard-sphere system. Kalos *et al.*[3] have also come to the conclusion that hard-sphere perturbation theory works well when studying the ground state of a Lennard-Jones model of ^{4}He. We arrive at a similar conclusion for finite temperature from our computation of the equations of state of ^{3}He and ^{4}He.

The helium pair potential is strongly repulsive at short range and weakly attractive at long range; with a minimum of approximately 10.8 K occurring at a pair separation near 2.95 Å. In this work we use the model pair potential of Aziz *et al.*[49] To develop the theory one takes the standard view that the repulsive core largely determines the structure of the solid or fluid and the attractive part may be treated as a perturbation. One divides the potential into a sum of repulsive and attractive contributions[52,53]

$$v(r)=v_{\rm rep}(r)+v_{\rm attr}(r) , \tag{60}$$

where

$$v_{\rm rep}(r)=\begin{cases} v(r)+\varepsilon, & r<r_m \\ 0, & r>r_m \end{cases} ,$$

$$v_{\rm attr}(r)=\begin{cases} -\varepsilon, & r<r_m \\ v(r), & r>r_m \end{cases} ,$$

and ε is the magnitude of the potential at its minimum r_m. The perturbative study done here involves two separate approximations. The first is to simply truncate the quantum statistical mechanical perturbation expansion of the free energy of the system of interest [$v(r)$] about that of the repulsive reference system [$v_{\rm rep}(r)$] after the first-order correction. The second, independent, approximation is to argue that the free energy and the pair-distribution function of the repulsive reference system are given accurately by those of an appropriately chosen hard-sphere system with the same mass, temperature, and density as the reference system. In other words, one adjusts the hard-sphere diameter at each temperature and density to "best" describe the reference system. This second approximation, or more precisely the problem of how to optimize the hard-sphere diameter, is on a much weaker theoretical foundation than its classical counterpart. In light of the absence of theoretical guidance, and in an effort to keep the number of adjustable parameters small, we have used the same, rather simple, hard-sphere model of the reference system as in the $T=0$ work of Ref. 3. The hard-sphere diameter is chosen so that its s-wave scattering length is equal to that of the reference system. This choice of diameter is thus independent of ρ and T. Initially, we considered matching the second virial coefficients of the two systems at each temperature [thereby making the equations of state of the two systems agree to $O(\rho^2)$ as $\rho\to 0$ for all T]. The two prescriptions turned out to be very nearly the same for the temperatures considered in this work. Clearly, either choice becomes poorer as the density is increased. As an extreme case, in *very* high density solid ^{4}He when the nearest neighbor distance is less than the above hard-sphere diameter the reference system certainly does not describe the ^{4}He system at all. We are presently attempting a quantum version of what has been done in the classical case,[53] namely, to construct a hard-sphere diameter $\sigma(\rho,T)$ that takes into account some of the many-body correlations and is therefore more accurate than the reference system used in this work. We will see below that the simple choice of hard-sphere reference system nevertheless provides rather accurate results for the Helmholtz free energy of ^{3}He and ^{4}He, except at the highest densities we have studied. It also gives a reasonable description of the freezing phenomenon and liquid-vapor coexistence in the helium systems.

The free energy per particle $f(\rho,T)$ for the system of interest is approximated by

$$f(\rho,T)\approx f^{(0)}(\rho,T)+f^{(1)}(\rho,T) , \tag{61}$$

where $f^{(0)}(\rho,T)$ is the free energy of the reference system,

$$f^{(1)}(\rho,T)=2\pi\rho\int_0^\infty v_{\rm attr}(r)g^{(0)}(r;\rho,T)r^2dr , \tag{62}$$

and $g^{(0)}$ is the pair distribution function of the reference

system. Equations (61) and (62) define f exactly to first order in the perturbation v_{attr}. As described in the previous paragraph, we make the additional approximations,

$$f^{(0)}(\rho,T)\approx f_{\text{HS}}(\rho,T) \tag{63a}$$

and

$$g^{(0)}(\rho,T)\approx g_{\text{HS}}(\rho,T)\ , \tag{63b}$$

where f_{HS} and g_{HS} are the free energy and pair-distribution function of the hard-sphere system with diameter σ equal to the scattering length of v_{rep}. We have computed $f^{(1)}(\rho,T)$ (using g_{HS}) at all the (ρ,T) points of this study with the scattering lengths of v_{rep} for both ^{3}He and ^{4}He. Let the two scattering lengths be σ_3 and σ_4. By integrating the two-body Schrödinger equation with zero angular momentum in the low-energy limit we find

$$\sigma_3=2.1634\ \text{Å},\quad \sigma_4=2.2033\ \text{Å}\ . \tag{64}$$

Rather than present tables of $f^{(1)}$ we choose to provide least-squares fits to $f^{(0)}+f^{(1)}$ as a function of ρ for each isotherm. The fit is

$$f^{(0)}+f^{(1)}=\sum_{l=0}^{3} c_l(\rho-\bar{\rho})^l \tag{65a}$$

in the solid, and

$$f^{(0)}+f^{(1)}=f_{\text{id}}(\rho,T)+\sum_{l=1}^{5} d_l\rho^l \tag{65b}$$

in the fluid. The coefficients c_l and d_l appear in the lower half of Table VIII. Note that the free energies of ^{3}He and ^{4}He are reduced by the unit $\hbar^2/m\sigma^2$ with the values m and σ of the corresponding isotope.

In Figs. 6(a), 6(b), and 6(c) we display the free energy computed by the perturbation theory for ^{4}He at temperatures 4, 10, and 20 K, along with the experimentally determined values from McCarty[54] in the fluid and Driessen *et al.*[55] in the solid. The "zeroth-order" theory may be defined by $f\approx f^{(0)}\approx f_{\text{HS}}$. From the figures one can see that the zeroth-order approximation is rather inaccurate, although the position of the fluid and solid free energy crossing is well represented. The inclusion of the first-order term $f^{(1)}$ removes almost all of the discrepancy from the experimental results, except at high density along the 20 K isotherm. It is remarkable that the simple choice of hard-sphere reference system gives quite accurate results over a rather wide range of conditions. If we had used the exact values of $f^{(0)}$ and $g^{(0)}$ rather than the hard-sphere approximations to them, then the estimate $f^{(0)}+f^{(1)}$ is a rigorous upper bound on f.[10] The use of f_{HS} and g_{HS} apparently does not destroy the upper-bound character for the cases considered here. Since the pressure is the slope of the free-energy curve; $P=\rho^2(\partial f/\partial\rho)$; we see that the first-order correction brings the pressure into good agreement with experiment. We find that for $\rho>0.2$ the *maximum* deviations of the pressure from experiment are roughly 15, 15, and 25% for the 4, 10, and 20 K isotherms, respectively. We expect similar results for ^{3}He although a lack of experimental data prevents us from performing a detailed comparison as is done for ^{4}He in Fig. 6.

Table XVII contains the melting-freezing parameters using the zeroth- and first-order perturbation theories for ^{3}He and ^{4}He along with the experimentally determined values of Grilly and Mills.[35] We first note that the coexisting densities, ρ_s and ρ_f, are fairly well determined by the zeroth-order approximation. In this case for both ^{3}He and ^{4}He along the $T=1.6$ and 4.0 isotherms the coexisting densities are no more than 4% in error, while for $T=8.0$ they are roughly 10% too small. The zeroth-order theory overestimates the coexistence pressure P_m. The first-order theory removes much of the discrepancy in P_m, at least for $T=1.6$ and 4.0. This is expected because the inclusion of the attractive part of the pair potential reduces the pressure substantially. At the lowest temperature the first-order perturbation brings the width of the transition $\Delta\rho=\rho_s-\rho_f$ into agreement with experiment, although this does not take place at the higher temperatures. In fact, the inclusion of the first-order correction does little to improve the densities ρ_s and ρ_f. We view this as a defect in the choice of hard-sphere diameter at densities near the transition region. It will be interesting to see if a more accurate hard-sphere mapping can be devised and to what extent it improves the equation of state and melting-freezing parameters.

One can see in Fig. 6(a) that the first-order theory for ^{4}He at $T=4$ K has an unstable region ($P<0$, $\partial P/\partial\rho<0$) in the fluid branch. This is an indication of the liquid-vapor phase transition. In Fig. 7 we replot the fluid free energy as a function of molar volume ($\sim 1/\rho$) to show the effect more clearly. Our perturbative free energies for ^{4}He at 10 and 20 K do not have an unstable region, which is quite reasonable because the liquid-vapor critical temperature for ^{4}He is $T_c=5.2$ K: there is no transition above this temperature.[31] Furthermore, the ^{3}He critical point is at 3.3 K and we observe no unstable region in any of our ^{3}He isotherms (5.5, 13.8, and 27.6 K). We have used the Maxwell double-tangent construction to locate the liquid-vapor coexistence at $T=4$ K for ^{4}He. This construction does *not* require any data in the unstable region, rather, it matches pressures and chemical potentials of the stable liquid and the stable vapor. The solid straight line in Fig. 7 is the resulting two-phase region and may be compared to the experimental values denoted by the dashed line.[54] We find that the coexistence volumes of the liquid and vapor are 28.9 and 355 cm^3, respectively, and the pressure is 0.827 atm. Experimentally, the values for these three quantities are 31.0 cm^3, 297 cm^3, and 0.808 atm, respectively. The agreement between simulation and experiment is very good. Note that this transition is quite close to the familiar boiling point of ^{4}He at $T=4.2$ K under atmospheric pressure.

VI. SUMMARY AND CONCLUSIONS

In this study we have shown the practicality of performing Monte Carlo free-energy calculations in quantum-mechanical many-body systems by path integrals. While we have computed the free energy for the hard-sphere system only, the several free-energy methods presented here are readily adaptable to other Hamiltoni-

ans of interest. The transition probability based on normal modes that we use to sample paths in the MRRTT algorithm is equally adaptable to other systems. We believe that with minor modifications (such as breaking up each path into "subpaths") this transition probability may be used effectively to study Boltzmann quantum systems at any temperature and density. As another technical point, we note that this work has demonstrated the utility and convergence properties of the image approximation to the high-temperature density matrix for many-body systems consisting of hard particles.

The free-energy computations allowed us to determine the two-phase coexistence between the solid and fluid at three temperatures. These data provide additional information about the hard-sphere phase diagram where previously only the $T=0$ and classical ($T\rightarrow\infty$) points were known. We have applied the hard-sphere perturbation theory to finite temperatures in the quantum regime and, by the use of a simple scattering length model, we have found good to excellent agreement with the experimental

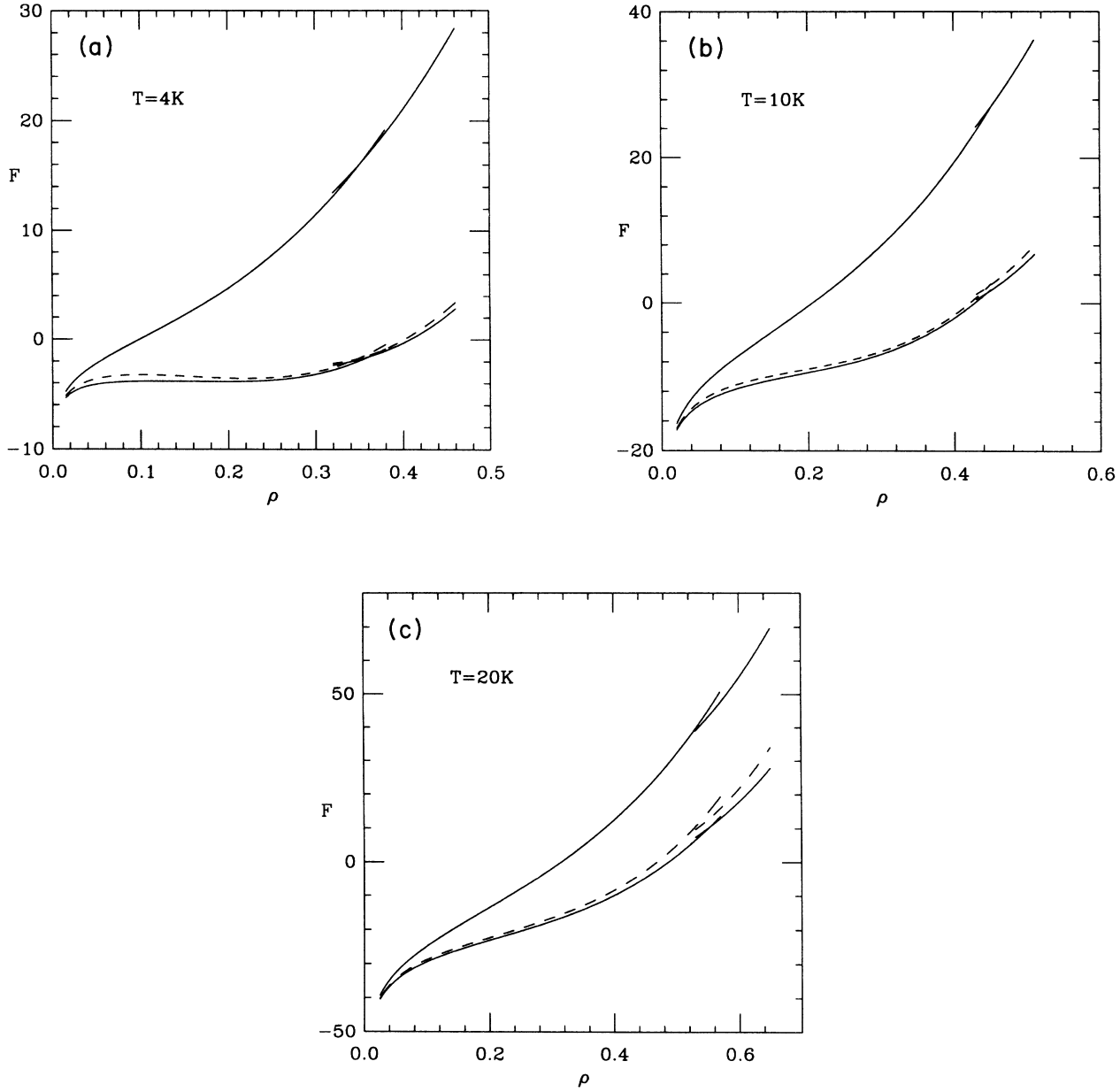

FIG. 6. (a) Comparison of the zeroth- and first-order hard-sphere perturbation-theory free energies and the experimental values for ^{4}He at a temperature of 4 K. Reduced units are used as explained in the text. For all three free energies both the fluid (low-density) and solid (high-density) branches are shown. The upper solid curves correspond to the zeroth-order theory that is the free energy of the hard-sphere system alone. The dashed curves are the hard-sphere free energy plus the first-order correction discussed in Sec. V. The lower solid curves are the experimental values for ^{4}He from the equations of state from Refs. 54 and 55. (b) Same as (a) except at 10 K. (c) Same as (a) except at 20 K; a sizable discrepancy between the hard-sphere perturbation theory (dashed curves) and the ^{4}He experimental values (lower solid curves) develops at high-density ρ in both the fluid and solid branches.

TABLE XVII. Perturbation theory parameters of the melting-freezing transition. The solid and fluid densities are ρ_s and ρ_f, respectively, of ^{3}He and ^{4}He for the three reduced temperatures T. The coexistence pressure is P_m and $\Delta\rho$ is $\rho_s-\rho_f$. HS(0) denotes the predictions of the zeroth-order theory using the hard-sphere free energy alone. HS(1) corresponds to the first-order hard-sphere perturbation theory described in Sec. V. "expt." is the experimentally determined values of Grilly and Mills in Ref. 35. All quantities are in the reduced units of the text.

	T	ρ_s	ρ_f	P_m	$\Delta\rho$
HS(0)	1.6	0.360	0.347	12.2	0.013
^{4}He HS(1)		0.365	0.341	3.7	0.022
^{4}He expt.		0.373	0.352	4.1	0.021
^{3}He HS(1)		0.357	0.339	5.3	0.018
^{3}He expt.		0.374	0.357	6.0	0.017
HS(0)	4.0	0.465	0.442	31.3	0.023
^{4}He HS(1)		0.461	0.432	16.8	0.029
^{4}He expt.		0.477	0.453	18.7	0.024
^{3}He HS(1)		0.460	0.434	20.2	0.026
^{3}He expt.		0.481	0.461	22.8	0.021
HS(0)	8.0	0.537	0.503	59.5	0.034
^{4}He HS(1)		0.537	0.496	41.0	0.041
^{4}He expt.		0.581	0.555	55.8	0.026
^{3}He HS(1)		0.538	0.498	45.7	0.041
^{3}He expt.		0.592	0.568	64.6	0.024

results for solid and fluid ^{3}He and ^{4}He in the equation of state, solid-fluid and liquid-vapor coexistence, and the elastic properties of the solid. It should be possible to find a more accurate hard-sphere mapping to improve further the agreement with experiment.

Our elastic study of the hard-sphere solid provides the first exact Monte Carlo determination of the elastic constants for a quantum solid (i.e., one dominated by zero-point motion). The results for the Debye temperatures of solid ^{3}He and ^{4}He are in fairly good agreement with experiment and we have shown that the experimentally observed ratio $\Theta_3/\Theta_4\approx 1.18$ can be described well by the combination of the scattering length model of helium, the scaling with mass of the hard-sphere system, and the Monte Carlo result for the hard-sphere Grüneisen constant. This result has a much stronger theoretical foundation than the standard explanation following from the harmonic approximation. We have demonstrated that the amount of thermal excitation in the solid at the densities and temperatures of this work can be semiquantitatively predicted from the Debye model (for a finite system) using the acoustic wave propagation velocities derived from the elastic constants we have computed. We have also shown that surprisingly good values for the total energy and Lindemann ratio are obtained from the substitution of our model phonon spectrum into the standard expressions of the harmonic theory.

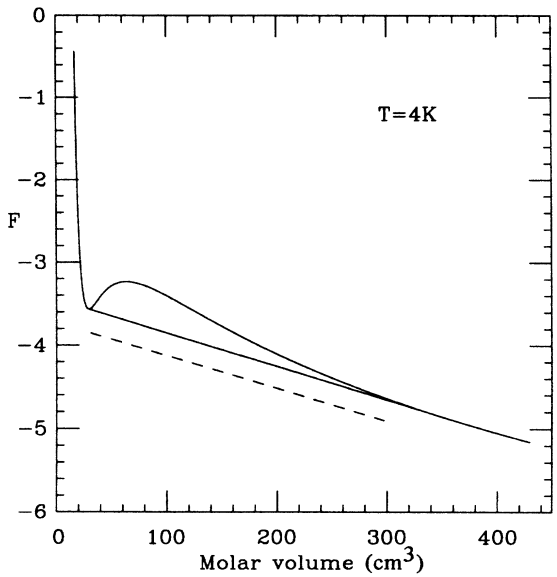

FIG. 7. Free energy vs molar volume near the liquid-vapor coexistence region at 4 K for ^{4}He. The solid curve is the result of the first-order hard-sphere perturbation theory. The solid line denotes the liquid-vapor coexistence as found by the Maxwell double-tangent construction. The straight dashed line is the experimental coexistence region for ^{4}He from Ref. 54. The free energy is in the reduced units of the text.

We would like to thank K.E. Schmidt, P.A. Whitlock, and M.H. Kalos for useful discussions. We also thank D. Sullivan and D. Eardley for assistance in the preparation of this manuscript. This research was supported by the National Science Foundation under Grant Nos. DMR-8513300 and DMR-81-17011. We acknowledge support from the NSF in a grant of computer time at the National Center for Superconducting Applications, Champaign, Illinois and the Cornell National Supercomputer Facility, Ithaca, New York.

ACKNOWLEDGMENTS

We would like to thank K.E. Schmidt, P.A. Whitlock, and M.H. Kalos for useful discussions. We also thank D.

Sullivan and D. Eardley for assistance in the preparation of this manuscript. This research was supported by the National Science Foundation under Grant Nos. DMR-8513300 and DMR-81-17011. We acknowledge support from the NSF in a grant of computer time at the National Center for Superconducting Applications, Champaign, Illinois and the Cornell National Supercomputer Facility, Ithaca, New York.

[1]N. Metropolis, A. W. Rosenbluth, M. N. Rosenbluth, A. H. Teller, and E. Teller, J. Chem. Phys. **21**, 1087 (1953).

[2]W. G. Hoover and F. H. Ree, J. Chem. Phys. **49**, 3609 (1968).

[3]M. H. Kalos, D. Levesque, and L. Verlet, Phys. Rev. A **9**, 2178 (1974).

[4]E. L. Pollock and D. M. Ceperley, Phys. Rev. B **30**, 2555 (1984).

[5]J. P. Hansen and I. R. McDonald, *Theory of Simple Liquids* (Academic, London, 1976).

[6]B. Jancovici, Phys. Rev. **178**, 295 (1969).

[7]The conclusion here relies on the absence of explicit spin-dependent terms in the Hamiltonian. In this case, in the temperature regime where statistics are unimportant, the *magnetic* degrees of freedom of the system decouple completely from the spatial degrees of freedom.

[8]L. H. Nosanow, in *Quantum Solids and Fluids,* edited by S. B. Trickey, E. D. Adams, and J. W. Duffy (Plenum, New York, 1977).

[9]This is not to say that the effects of statistics cannot be seen in *any* property of the solid. For example, in solid ^{3}He, the infrequent atomic exchanges give rise to a very weak (~ 1 mK) exchange interaction between the nuclear spins. This interaction leads to the very diverse magnetic phases of the solid.

[10]R. P. Feynman, *Statistical Mechanics* (Benjamin, New York, 1972); R. P. Feynman and A. R. Hibbs, *Quantum Mechanics and Path Integrals* (McGraw-Hill, New York, 1965).

[11]K. S. Schweizer, R. M. Stratt, D. Chandler, and P. G. Wolynes, J. Chem. Phys. **75**, 1347 (1981).

[12]D. Chandler and P. G. Wolynes, J. Chem. Phys. **74**, 4078 (1981).

[13]Strictly speaking, our notation should distinguish between actual quantum-mechanical averages, Eq. (4), and averages in the "effective" classical system, Eq. (16); hopefully, the context shall make it clear which average is meant.

[14]J. Barker, J. Chem. Phys. **70**, 2914 (1979).

[15]G. Jacucci and E. Omerti, J. Chem. Phys. **79**, 3051 (1983).

[16]L. W. Bruch, I. J. McGee, and R. O. Watts, Phys. Lett. **50A**, 315 (1974).

[17]D. M. Ceperley and E. L. Pollock, Phys. Rev. Lett. **56**, 351 (1986).

[18]G. Jacucci, in *Monte Carlo Methods in Quantum Problems,* edited by M. H. Kalos (Reidel, Holland, 1982).

[19]T. L. Hill, *Statistical Mechanics* (McGraw-Hill, New York, 1956).

[20]M. Fierz, Phys. Rev. **106**, 412 (1957).

[21]M. H. Kalos and P. Whitlock, *Monte Carlo Methods* (Wiley, New York, 1986), Vol. I, pp. 103–107.

[22]J. P. Valleau and G. M. Torrie, in *Statistical Mechanics A, Modern Theoretical Chemistry,* edited by B. J. Berne (Plenum, New York, 1977), Vol. 5.

[23]J. D. Doll, R. D. Coalson, and D. L. Freeman, Phys. Rev. Lett. **55**, 1 (1985).

[24]M. Rao and B. J. Berne, J. Chem. Phys. **71**, 129 (1979).

[25]Our method may be compared to those of Ceperly and Pollock in Refs. 4 and 17 and the method that appears in M. Takahashi and M. Imada, J. Phys. Soc. Jpn. **53**, 963 (1984).

[26]D. Levesque, J. J. Weis, and J. P. Hansen, in *Monte Carlo Methods in Statistical Physics,* edited by K. Binder (Springer-Verlag, Berlin, 1979), Chap. 2.

[27]M. E. Boyd, S. Y. Larsen, and J. E. Kilpatrick, J. Chem. Phys. **45**, 499 (1966).

[28]D. Frenkel and A. Ladd, J. Chem. Phys. **81**, 3188 (1984).

[29]The $T=1.6$ isotherm was actually performed at $T=1.6002$.

[30]N. W. Ashcroft and N. D. Mermin, *Solid State Physics* (Holt, New York, 1976), Chap. 23.

[31]J. Wilks, *The Properties of Liquid and Solid Helium* (Clarendon, Oxford, 1967).

[32]W. H. Press, B. P. Flannery, S. A. Teukolsky, and W. T. Vetterling, *Numerical Recipes* (Cambridge University Press, Cambridge, 1986), Chap. 14.

[33]One must take care since the resulting variance may depend strongly on the choice of least-squares-fitting function used and thus the variance may not measure the "true" error in $f(\rho)$.

[34]M. H. Kalos, M. A. Lee, P. A. Whitlock, and G. V. Chester, Phys. Rev. B **24**, 115 (1981).

[35]E. R. Grilly and R. L. Mills, Ann. Phys. (N.Y.) **8**, 1 (1959).

[36]F. A. Lindemann, Z. Phys. **11**, 609 (1910).

[37]P. A. Whitlock, D. M. Ceperley, G. V. Chester, and M. H. Kalos, Phys. Rev. B **19**, 5598 (1979).

[38]J. P. Hansen and D. Levesque, Phys. Rev. **165**, 293 (1968).

[39]D. M. Ceperley, Phys. Rev. B **18**, 3126 (1978).

[40]D. A. Young and B. J. Alder, J. Chem. Phys. **60**, 1254 (1974).

[41]Of course some modification must be made for the one-component plasma where the scattering length is not defined.

[42]See, however, R. Mochkovitch and J. P. Hansen, Phys. Lett. **73A**, 35 (1979) for a study of the effect of statistics using a generalized Lindemann criterion for the reentrant solid-fluid phase transition of the one-component plasma.

[43]K. E. Schmidt, M. A. Lee, M. H. Kalos, and G. V. Chester, Phys. Rev. B **24**, 115 (1981).

[44]H. R. Glyde, in *Rare Gas Solids,* edited by M. L. Klein and J. A. Venables (Academic, New York, 1976), Chap. 7; L. W. Bruch and J. M. Gottlieb, Phys. Rev. B **37**, 4920 (1988).

[45]D. C. Wallace, in *Solid State Physics,* edited by H. Ehrenreich, F. Seitz, and D. Turnbull (Academic, New York, 1970), Vol. 25, p. 301.

[46]K. J. Runge and G. V. Chester, Phys. Rev. A **36**, 4852 (1987).

[47]D. Frenkel and A. Ladd, Phys. Rev. Lett. **59**, 1169 (1987).

[48]H. H. Sample and C. A. Swenson, Phys. Rev. **158**, 188 (1967).

[49]R. A. Aziz, V. P. S. Nain, J. S. Carley, W. L. Taylor, and G. T. McConville, J. Chem. Phys. **70**, 4330 (1979).

[50]In actuality we observe a deviation in γ_0 of about 20% over the range of densities studied. A better fit is $\ln\theta^*=4.961+2.020(\ln\rho^*)-0.6174(\ln\rho^*)^2$.

[51]However, it will be shown below that the standard harmonic theory zero-point values are not more than 50% off of the exact results for the three densities studied.

[52]J. D. Weeks and D. Chandler, Phys. Rev. Lett. **25**, 149 (1970); J. D. Weeks , D. Chandler, and H. C. Andersen, J. Chem. Phys. **54**, 5237 (1971); **55**, 5422 (1971).

[53]J. A. Barker and D. Henderson, Rev. Mod. Phys. **48**, 587

(1976).
[54]R. D. McCarty, J. Phys. Chem. Ref. Data **2**, 923 (1973).
[55]A. Driessen, E. van der Poll, and I. F. Silvera, Phys. Rev. B **33**, 3269 (1986).
[56]D. M. Ceperley (private communication).